Faculteit Industriële Ingenieurswetenschappen

master in de industriële wetenschappen: energie

Masterthesis

Best suited device architectures and selective contacts for thin film van der Waals materials based on Sb_2Se_3 chalcogenide and SbSeI chalcohalide compounds

Sander Moens

Scriptie ingediend tot het behalen van de graad van master in de industriële wetenschappen: energie

PROMOTOR :
Prof. dr. Bart VERMANG

PROMOTOR :
Prof. dr. Edgardo SAUCEDO

Gezamenlijke opleiding UHasselt en KU Leuven

Universiteit Hasselt | Campus Diepenbeek | Faculteit Industriële Ingenieurswetenschappen | Agoralaan Gebouw H - Gebouw B | BE 3590 Diepenbeek

Universiteit Hasselt | Campus Diepenbeek | Agoralaan Gebouw D | BE 3590 Diepenbeek
Universiteit Hasselt | Campus Hasselt | Martelarenlaan 42 | BE 3500 Hasselt

2022
2023

Faculteit Industriële Ingenieurswetenschappen

master in de industriële wetenschappen: energie

Masterthesis

Best suited device architectures and selective contacts for thin film van der Waals materials based on Sb_2Se_3 chalcogenide and SbSeI chalcohalide compounds

Sander Moens

Scriptie ingediend tot het behalen van de graad van master in de industriële wetenschappen: energie

PROMOTOR :

Prof. dr. Bart VERMANG

PROMOTOR :

Prof. dr. Edgardo SAUCEDO

UHASSELT KU LEUVEN

Preface

As I embark on the final stages of my research journey on thin film solar cells, I am filled with a sense of accomplishment and gratitude. I would like to begin by thanking my supervisors, Prof. Dr. Saucedo Edgardo and Prof. Dr. Vermang Bart for their unwavering support and guidance throughout this project. Their expertise in the field of photovoltaics and their willingness to mentor me have been instrumental in shaping the direction of my research and have provided me with a deeper understanding of the subject matter. Their patience, encouragement and constructive feedback have been invaluable, and I am honored to have had the opportunity to work under their guidance. I would also like to extend my gratitude to my girlfriend, family and friends, who have been my constant source of love, support and motivation throughout this international exchange.

Finally, I would like to acknowledge the contributions of my lab colleagues who have played an essential role in this research. The knowledge, skills and expertise shared in our discussions have helped to bring new insights and perspectives to my work. I am deeply grateful for the opportunity to have worked with such a talented and dedicated team that I can now call friends. I hope that this thesis will make a valuable contribution to the field of thin film solar cells and pave the way for future research in this exciting and rapidly growing area.

Table of contents

Preface 1
List of figures 5
Abbreviations 7
Abstract 9
Abstract in Dutch 11
1 Introduction 13
2 Literature review 15
2.1 pn-junction 15
2.1.1 Depletion region 15
2.1.2 Homo- and heterojunctions 16
2.1.3 Energy band diagram 16
2.2 Solar cells 17
2.2.1 Working principle 17
2.2.2 Band alignment 18
2.3 Thin-film solar cells 19
2.3.1 Practical synthesis 20
2.3.2 Chalcogenides 21
2.3.3 Metal chalcohalides 22
2.4 Conclusion 22
3 Experimental procedures 23
3.1 Workplan 23
3.2 Synthesis plan 24
3.3 Synthesis of devices 25
3.3.1 Chemical vapor deposition (CVD) 25
3.3.2 Physical vapor deposition (PVD) 27
3.3.3 Chemical bath deposition (CBD) for CdS 29
3.3.4 Low-pressure annealing for post-selenization 30
3.3.5 High pressure high pressure annealing for iodination 31
3.3.6 Spin coating of PEDOT:PSS 32
3.3.7 Diamond point scribing and indium (In) soldering 33
3.4 Characterization 34
3.4.1 Solar simulator 34
3.4.2 Scanning electron microscopy (SEM) 37
3.4.3 External quantum efficiency (EQE) 38
3.4.4 X-ray diffraction (XRD) 40
4 Results and discussion 41
4.1 Optoelectronic measurements 41
4.1.1 Efficiency 41
4.1.2 Open-circuit voltage and short-circuit current 42
4.1.3 Fill factor 42
4.1.4 External quantum efficiency 43
4.1.5 Discussion 44
4.2 SEM imaging 47
4.2.1 Discussion 54
4.3 XRD measurements 55
4.3.1 Discussion 55
5 Conclusion 56
5.1 Future work 56

References 57
Appendices 59

List of figures

Figure 1: Substrate configuration and superstrate configuration 13
Figure 2: UPC and the SENSATE project logo's 13
Figure 3: Creation of depletion region at the PN-junction 15
Figure 4: PN-junction schematic and band diagram 15
Figure 5: Simplified band diagram of an insulator, semiconductor and conductor 16
Figure 6: Solar cell working principle 17
Figure 7: Bandgap alignment with a positive CBO 18
Figure 8: Bandgap alignment with a negative CBO 19
Figure 9: Configuration of a practical thin-film device 20
Figure 10: Potential solar spectrum absorption for tandem devices 20
Figure 11: Columnar structure of Sb_2Se_3 and grains 21
Figure 12: Cross section of SbSeI deposition showing non-parallel columnar structures 22
Figure 13: Different layers for substrate configuration devices 23
Figure 14: Different layers for superstrate configuration devices 23
Figure 15: Original synthesis plan of all planned devices 24
Figure 16: Thermal evaporation principle 25
Figure 17: Kenosistec system and the open co-evaporation chamber 26
Figure 18: An Opened ALD reaction chamber with samples and a complete ALD system 26
Figure 19: Thermal evaporation system inside a glovebox and sample holder with grid masks 27
Figure 20: Sputtering principle 28
Figure 21: CdS CBD principle and CBD setup at the PV-group 29
Figure 22: Nabertherm low pressure furnace 30
Figure 23: post-selenization principle 30
Figure 24: SbSeI formation principle 31
Figure 25: Prepared Petri dish (left) and the MTI High pressure furnace 31
Figure 26: PEDOT solvent, sample holder and spin coater 32
Figure 27: Diamond point and scribed device 33
Figure 28: Indium solder on FTO for superstrate devices and In solder on the Mo for substrate devices 33
Figure 29: Solar photon flux on earth's surface and corresponding bandgap energies 34
Figure 30: JV-curve and power density for bandgap energies E_g= 0,8; 1,4 and 2,0 eV and the conversion efficiency in function of E_g in the SQ limit 35
Figure 31: G2V Optics Pico and sample SUB-1 connected to the probes 36
Figure 32: SEM principle and the SEM at UPC 37
Figure 33: Example of losses in a tandem device 38
Figure 34: EQE measurement equipment using a monochromator 38
Figure 35: Example of EQE measurement 39
Figure 36: XRD setup of the source and detector 40
Figure 37: Constructive interference and Bruker D8 Advance diffractometer 40
Figure 38: Substrate device efficiencies 41

Figure 39: Superstrate device efficiencies 41
Figure 40: V_{oc} and J_{sc} of SUB-5 and SUPER-18 42
Figure 41: Efficiency and Fill factor of SUB-5 and SUPER-18 42
Figure 42: EQE plot of SUB-5 43
Figure 43: Comparing SUB-1 to previously synthesized devices at 2 bar and different iodination temperatures 44
Figure 44: Cross sectional SEM images of devices at different iodination temperatures 45
Figure 45: Formation of shunt path 45
Figure 46: Cross sectional SEM image of SUB-5 47
Figure 47: Top view SEM image of SUB-5 47
Figure 48: Top view SEM image of SUB-5 in the Ag grid region 48
Figure 49: Cross sectional SEM image from SUB-1 48
Figure 50: Top view SEM image of SUB-1 49
Figure 51: Cross sectional SEM image of SUB-6 49
Figure 52: Cross sectional SEM image of SUB-3 50
Figure 53: Top view SEM images of SUB-3 51
Figure 54: Cross sectional SEM image of SUPER-18 52
Figure 55: Cross sectional SEM image of SUPER-18 in the Ag contact region 52
Figure 56: Cross sectional SEM image of SUPER-16 53
Figure 57: Cross sectional SEM image of SUPER-8 54
Figure 58: Diffractogram of SUB-2, SUB-6, SUPER-12 and SUPER-28 55

Abbreviations

Å	Ångström
Ag	Silver
Au	Gold
ALD	Atomic Layer Deposition
Bi_2Se_3	Bismuth selenide
BIPV	Building Integrated Photovoltaics
C	Carbon
CBD	Chemical Bath Deposition
CBO	Conduction Band Offset
$Cd(NO_3)_2$	Cadmium nitrite
CdS	Cadmium sulfide
CVD	Chemical Vapor Deposition
LPCVD	Low-pressure CVD
E_c	Lowest conduction band energy
E_{Fp}	Fermi level of P-type material
E_{Fn}	Fermi level of N-type material
E_g	Bandgap energy
E_{photon}	Photon energy
E_v	Highest valence band energy
EQE	External Quantum Efficiency
ETL	Electron Transport Layer
EU	European Union
FF	Fill Factor
FTO	Fluor-doped tin oxide
GB	Grain Boundaries
H_2O	Dihydrogen oxide (water)
HTL	Hole Transport Layer
IREC	Fundación Instituto de Investigación de la Energía de Cataluña
In	Indium
J_{sc}	Short-circuit current
LED	Light Emitting Diodes
Mo	Molybdenum
MoO_3	Molybdenum trioxide
$Na_3C_6H_5O_7$	Sodium citrate
NH_3	Ammonia
PCE	Power Conversion Efficiency
PEDOT:PSS	poly(3,4-ethylenedioxythiophene) polystyrene sulfonate
PID	Proportional Integral Derivative
PV	Photovoltaics
PVD	Physical Vapor Deposition
QCM	Quartz Crystal Microbalance
Sb_2Se_3	Antimony selenide
SbSeBr	Antimony selenobromide
SbSeI	Antimony selenoiodide
$SC(NH_2)_2$	Thiourea
SEM	Scanning Electron Microscopy
SET	Strategic Energy Technology
SLG	Soda Lime Glass

SQ	Shockley-Queisser
TCO	Transparent Conductive Oxide
TiO_2	Titanium dioxide
UPC	Universitat Politècnica de Catalunya
V_{oc}	Open-circuit voltage
V_2O_5	Vanadium Pentoxide
VBM	Valence Band Minimum
Xe	Xenon
XRD	X-ray Diffraction

Abstract

Thin film solar cells have become a hot topic for their interesting applications in building integrated photovoltaics (BIPV) and the possibility to achieve higher efficiencies with multi-junction devices by combining them with existing PV technologies. A big focus lays on the development of these technologies from environmentally friendly materials to ensure safety and sustainability. chalcogenides, like antimony selenide (Sb_2Se_3) and metal chalcohalides, like antimony selenoiodide (SbSeI), share these advantages and show useful wide bandgap properties for PV applications.

SbSeI is an emerging thin film material and has limited research on device architecture and electron/hole selective contacts. This master's thesis will mainly be focused on the synthesis of different possible device configurations by comparing them to a reference absorber material like Sb_2Se_3. By using proven materials as selective contact such as cadmium sulfide (CdS), titanium dioxide (TiO_2) and vanadium pentoxide (V_2O_5) as electron transport layers (ETL) and molybdenum (Mo), molybdenum trioxide (MoO_3) and PEDOT as hole transport layers (HTL). All these materials are deposited using existing techniques such as sputtering, thermal evaporation, annealing, spin coating, atomic layer deposition (ALD) and chemical bath deposition (CBD). For characterization, the JV-curves are measured with a solar simulator, top view and cross-sectional images are taken by scanning electron microscopy (SEM), together with X-ray diffraction (XRD) measurements.

With current process parameters the absorber material SbSeI grows in columnar structures. These columns can grow up to 10's micrometers in a random orientation, resulting in an uneven surface morphology. Reacting all of the precursor also creates a worsening coverage of the underlying contact layer, which increases shunt paths. Lastly, the structures seem to be very fragile to outside forces. Due to the centrifugal forces of spin coating, a number of structures are damaged or broken. The measurement probe contact point also seems to damage a larger area of the device surface, which could influence measurements.

Abstract in Dutch

Dunne-film zonnecellen zijn een veelbesproken onderwerp vanwege hun interessante toepassingen in building integrated photovoltaics (BIPV) en de mogelijkheid om hogere rendementen te bereiken met multi-junction cellen door deze te combineren met bestaande PV-technologieën. Een grote nadruk ligt op de ontwikkeling van deze technologieën uit milieuvriendelijke materialen om veiligheid en duurzaamheid te waarborgen. Chalcogenides, zoals antimoon triselenide (Sb_2Se_3) en metal chalcohalides, zoals antimoon selenium jodide (SbSeI), delen deze voordelen en vertonen nuttige brede bandgap eigenschappen voor PV-toepassingen.

SbSeI is een opkomend dunne film materiaal met beperkt onderzoek naar apparaat architectuur en elektron/gaten selectieve contacten. Deze masterproef zal voornamelijk gericht zijn op de synthese van verschillende mogelijke apparaten configuraties door ze te vergelijken met een referentie-materiaal zoals Sb_2Se_3. Door materialen te gebruiken als selectief contact zoals cadmiumsulfide (CdS), titaniumdioxide (TiO2) en vanadiumpentoxide (V2O5) als elektronentransportlagen (ETL) en molybdeen (Mo), molybdeentrioxide (MoO3) en PEDOT als gatentransportlagen (HTL). Al deze materialen worden in lagen afgezet met bestaande technieken zoals sputteren, thermal evaporation, annealing, spin coating, atomic layer deposition (ALD) en chemical bath deposition (CBD). Voor de karakterisering worden de JV-curven gemeten met een zonnesimulator, bovenaanzicht- en doorsnedebeelden gemaakt met behulp van scanning electron microscopy (SEM) en X-ray diffractogram (XRD) metingen gedaan.

Met de huidige procesparameters blijkt het absorptiemateriaal SbSeI te groeien in kolomvormige structuren. Deze kolommen kunnen groeien tot 10's micrometer in een willekeurige oriëntatie, wat resulteert in een ongelijke oppervlaktemorfologie. Wanneer alle precursor reageert in de reactie ontstaat ook een slechtere dekking van de onderliggende laag, waardoor de shuntpaden toenemen. Ten slotte lijken de structuren zeer kwetsbaar voor krachten van buitenaf. Door de centrifugale krachten van spin coating is een aantal structuren beschadigd of gebroken. Het contactpunt van de meetsonde lijkt ook een groter gebied van het oppervlak te beschadigen, wat de metingen zou kunnen beïnvloeden.

1 Introduction

According to [1], the Strategic Energy Technology Plan (SET plan) by the EU is to achieve a share of 75% of renewable electricity by 2050. Photovoltaic (PV) energy is recognized as one of the strong candidates to achieve the goals of this plan. Currently, market dominant single junction PV cells are based on silicon (Si) due to a high power conversion efficiency (PCE) of 26% in laboratory environment. [2] states that this value approaches the thermodynamic limit for single PV junction cells. To further enhance solar cell performance, innovative technologies are considered. Tandem technology uses double stacked cells to achieve efficiencies up to 38.8%.

The development of high quality wide bandgap materials, generally used as a top cell, is crucial for even higher tandem cell performance. According to [3], semi-transparent properties make it interesting for building integrated PV (BIPV) applications. Antimony selenoiodide (SbSeI) and antimony selenobromide (SbSeBr) based on antimony selenide (Sb_2Se_3) as a precursor, have shown to be excellent absorbers with a wide bandgap, stable and relatively low processing temperatures. In laboratory environment Sb_2Se_3 has already showed high PCE without little research effort, indicating a huge potential for advanced PV concepts. These absorber materials have limited research on optimal device structure and compatible partner layers, more specifically the deposition of different type selective contacts, including electron transport layers (ETL) and hole transport layers (HTL).

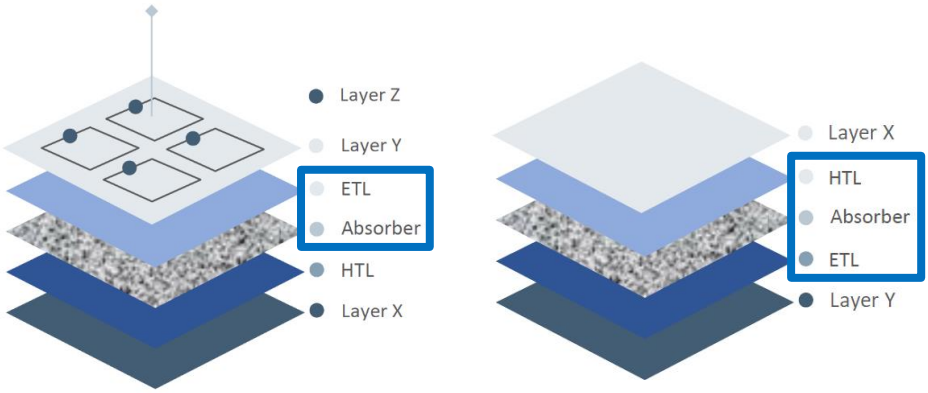

Figure 1: Substrate configuration (left) and superstrate configuration (right) (Appendix A).

The photovoltaic group at UPC (Universitat Politècnica de Catalunya) does research on this topic under the SENSATE project supported by the EU [3]. By using state of the art technology and innovative materials, different device architectures are produced in an iterative way to achieve the highest possible efficiency.

UNIVERSITAT POLITÈCNICA DE CATALUNYA BARCELONATECH

SENSATE

Figure 2: UPC and the SENSATE project logo's [3].

2 Literature review

2.1 pn-junction

Combining a p-type and n-type semiconductor (where majority carriers are holes and electrons, respectively) creates a pn-junction and sets the basis for the explanation of the working principle of solar cells. This topic is further explained using information and concepts from [4] and [5].

2.1.1 Depletion region

The different electron and hole concentrations between these types, results in the diffusion of carriers through the junction until thermodynamic equilibrium is reached. Part of the free majority charge carriers from the both regions diffuse to the other side of the junction and combine with the (other) majority carriers (recombination), leaving behind negative/positive ions in the p/n-region. This leads to the formation of a region depleted of carriers, called the depletion region [4].

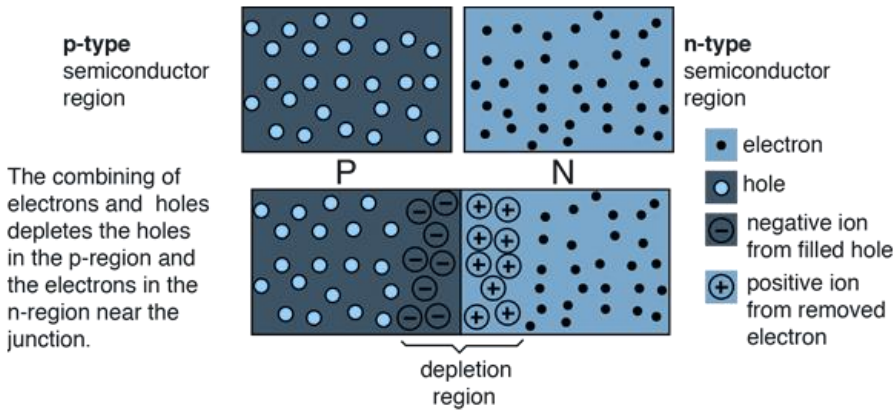

Figure 3: Creation of depletion region at the PN-junction [6].

The forming of this depletion region can be shown by an energy band diagram. Initially, the Fermi levels of the two semiconductor types will be different due to the different doping. As a consequence, a drift of majority carriers in opposite directions happens. The Fermi levels will eventually equalize by reaching a steady state condition. The use of different alignment of bands (conduction for electron and valence for holes) can lead to some advantageous properties for solar cells, such that specific charge carriers are 'selected' to pass. In other words, creating a selective contact for either holes or electrons depending on the materials used [4].

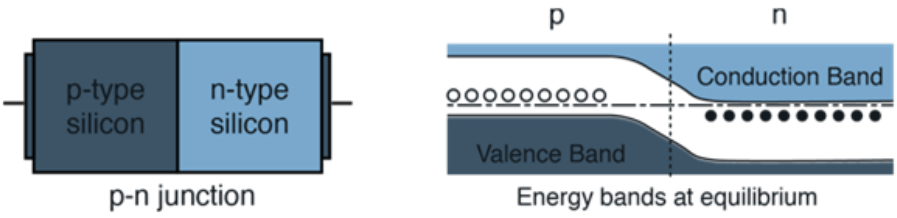

Figure 4: PN-junction schematic (left) and band diagram (right) [6].

2.1.2 Homo- and heterojunctions

The previously mentioned pn-junction consists of an n-type and p-type of the same semiconductor and is thus called a homojunction. Alternatively, when different semiconductors are combined to form a junction (with corresponding energy band diagrams), these are called heterojunctions [4].

2.1.3 Energy band diagram

A single Si atom has 3 definite energy states where a certain number of electrons are present. The number of energy states depends on the type of atom. Creating a solid structure from intrinsic Si results in interaction between orbitals of neighboring Si atoms. This interaction creates a range of energy states for electrons to occupy called energy bands. Only the highest energy state of valence electrons experience this interaction and therefore, this is relevant to model solar cells. Lower energy states are practically not affected in a solid. Exciting an electron can result in it becoming a free electron in the band generated by the lowest unoccupied orbitals of the solid. In between these energy states is a gap, in which in an ideal case no electronic states exist. This gap is a distinct feature of a semiconductor [5].

The upper band is the conduction band, and the lower band is called the valence band. The forbidden gap region between the highest valence band and the lowest conduction band is known as the bandgap or energy gap E_g [eV]. Electron energy is defined on the Y-axis. Higher conduction or valence bands mean higher electron energy. For solar cells, the most relevant properties of these bands are E_v (= highest valence band energy state) and E_c (= lowest conduction band energy state) [5].

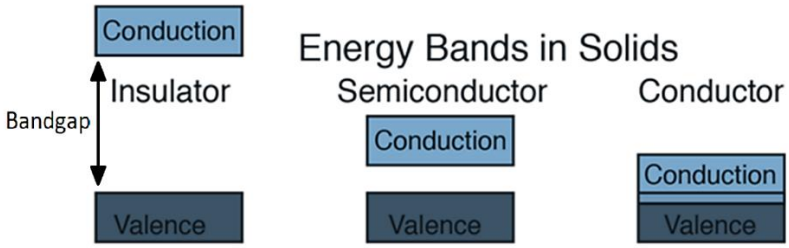

Figure 5: Simplified band diagram of an insulator, semiconductor and conductor [7].

2.2 Solar cells

The following topic is explained using information and topics from [8] and [9].

2.2.1 Working principle

The main principle of a solar cell is to create a charge flow that can be used to power a device. To describe this, we use a combination of all previously mentioned topics. When a photon with sufficient energy excites an electron in the valence band, the electron jumps to the conduction band leaving behind a hole in the valence band [8].

After generation, in order to generate a current, each charge carrier has to be collected at specific contacts. For this, specific material layers are used as selective filters of either holes or electrons. Despite other factors affecting the result, the most commonly used method is by using n-type materials to select electrons and p-type materials to select holes. This layers are called electron and hole transport layers (ETL and HTL respectively) [8].

Also, the generation of electron-hole pairs implies an out of equilibrium state, in this case the increased number of electrons and holes at the conduction and valence band are indicated by the quasi-Fermi levels, where E_{Fn} is the electron level and E_{Fp} is the holes level. The difference in these levels is the maximum open circuit voltage V_{oc} [8].

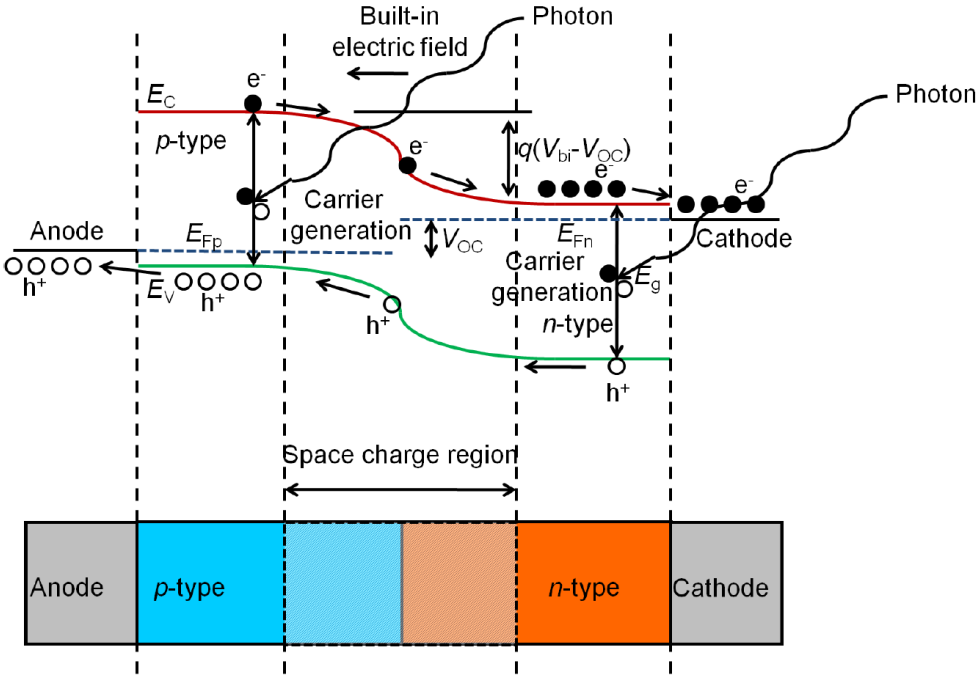

Figure 6: Solar cell working principle [8].

2.2.2 Band alignment

Band alignment is an important parameter to consider when designing solar cell configurations. Band alignment of certain materials can change the form of the junction. Two separate materials can have a specific band structure when not combined. But once combined the Fermi-levels will align and a band offset will occur in both the conduction and valence band, depending on the type of material. For instance, a spike-like conduction band offset (CBO) occurs when the conduction band minimum (CBM) of the selective contact is higher than the conduction band of the absorber. In case the window layer has a lower conduction band than the absorber conduction band, a more cliff-like offset will occur. The same can happen to the valence band maximum (VBM) [9].

Positive band offset

When a photon excites an electron in the absorber the electron moves up to the conduction band. The function of the transport layer is to extract the electrons/holes from the absorber conduction/valence band. But with a positive CBO, the carriers will encounter a barrier. This makes drift into the selective contact more difficult and thus the short-circuit current J_{sc} decreases resulting in lower efficiency [9].

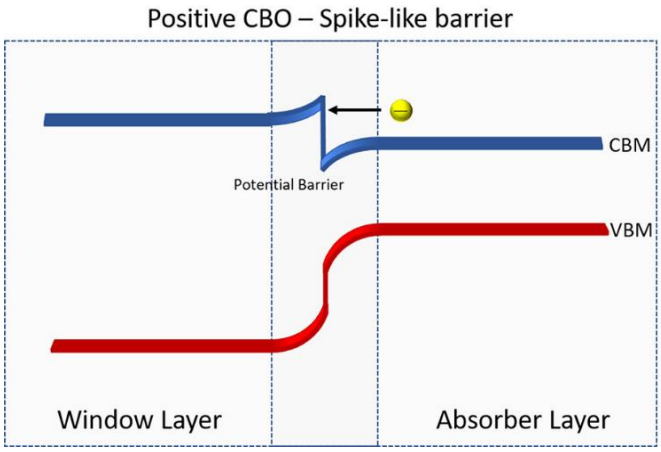

Figure 7: Bandgap alignment with a positive CBO [9].

Negative band offset

A negative CBO creates a steep slope or cliff-like offset. Because of the bandgaps being quite close to each other and thus smaller, electron-hole recombination takes place at the interface. This results in a lower V_{oc} in the detriment efficiency. The quasi-Fermi levels are very close to each other leading to a lower V_{oc}. A good band alignment is needed to optimize J_{sc} and V_{oc} to increase cell performance. This can be done through simulation tools like SCAPS, before synthesizing devices [9].

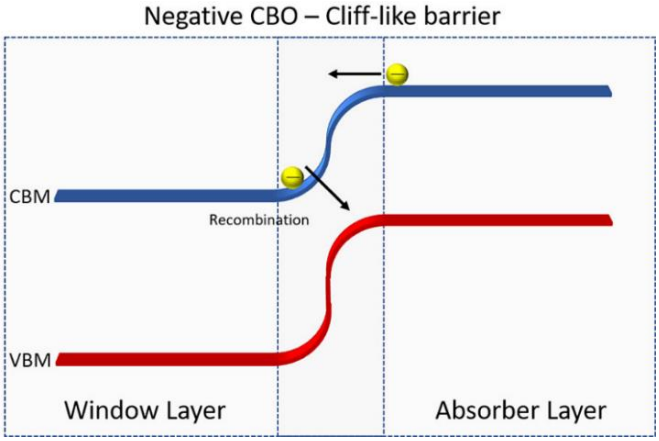

Figure 8: Bandgap alignment with a negative CBO [9].

2.3 Thin-film solar cells

According to [10], First generation solar cells are long dominated by crystalline silicon and are wildly adopted for commercial purposes. The cells consist of Si wafers that are hundreds of micrometers thick. Thin-film solar cells, however, are second generation cells with thicknesses that range from nano- to tens of micrometers. These cells consist of multiple thin-film layers deposited on top of a sub- or superstrate like Soda Lime Glass (SLG). Because of the smaller thickness, these types of cells are more interesting for specific purposes like-building integrated PV, flexible PV etc. Some materials show semi-transparent properties indicating the possible usage of thin film as top cell for tandem cell configurations to capture a wider range of photon energies, and significantly increase device efficiency [10].

2.3.1 Practical synthesis

A real world a solar cell not only consists of an ETL and HTL, although it would technically work. Higher efficiencies are achieved by combining different layers to maximize electron-hole generation and extract them with minimal losses. The synthesis of a thin-film solar cell starts from the sub- or superstrate, which creates the base for all following layers. For instance, a device in substrate configuration would start from a soda lime glass (SLG) base. Upon this base an HTL also called the back contact would be deposited. Then the absorber follows, this is where most of the photons will be absorbed to create electron-hole pairs. The next layers make up the front contact, this consists of the ETL, a transparent conductive oxide (TCO) and a metallic grid to extract the electrons (see Appendix A).

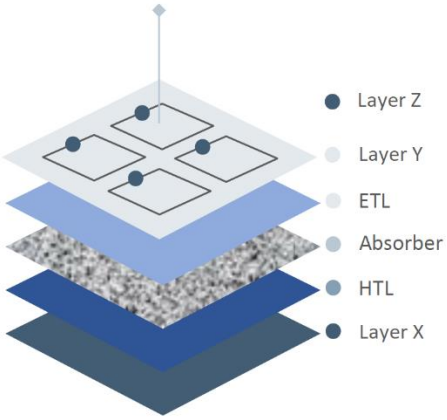

Figure 9: Configuration of a practical thin-film device (see Appendix A).

[4] states that even higher efficiencies are achieved when creating multi-junction devices, which consist of the above configuration, but with a second (or more) device deposited on top. In this case the device consists of a bottom- and top cell, with each a different optimal bandgap. The difference in bandgap allows for a wider range of photon absorption, and thus higher electron-hole generation on the same surface area. This substantially increases device efficiencies [4].

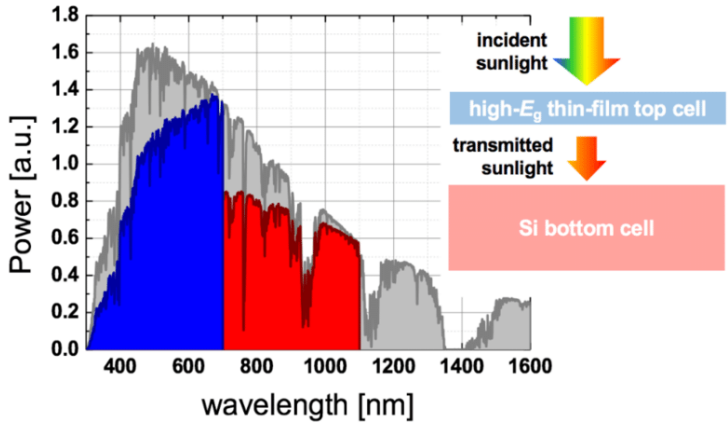

Figure 10: Potential solar spectrum absorption for tandem devices [11].

2.3.2 Chalcogenides

Combining one (or more) electropositive element and one (or more) chalcogen anion creates a chalcogenide. [12] states that chalcogenides based on sulfides and selenides have shown promising results in low-cost, high-efficiency PV applications. These materials have been studied for a longer period compared to chalcohalides, showing promising results [12].

Antimony Selenide

According to [13], among the chalcogenides, antimony selenide (Sb_2Se_3) has shown interesting properties. The optimal bandgap, high absorption coefficient, non-toxicity, earth-abundant and electrical properties make this material a suitable candidate for PV applications. A single junction solar cell could theoretically reach up to 30% using this material. For thin-films up to 500nm, Sb_2Se_3 shows good a good absorption coefficient in the visible spectrum. Leading to potential higher power conversion efficiency (PCE) [13].

Quasi-1D structures

[13] states that the unique structure of Sb_2Se_3 is a quasi-1D crystal structure. The columns are built with strong covalent bonds among the atoms. In between, the columns are held together by weak forces due to Van der Waals interaction. These forces are dependent on the distance between atoms and molecules. This is a significant difference compared to more traditional bulk materials used in PV applications, such as Si. These structures have a lot of advantages when orientated in a perpendicular way with respect to the substrate. The columnar structures show less recombination losses because of the lack of presence of dangling bonds on the structure surface and at grain boundaries (GB). Resulting in a more inert surface compared to bulk materials. More enhanced electrical properties are present in the parallel direction of the ribbon. However, as previously mentioned this advantage is only present when all structures are correctly oriented [13].

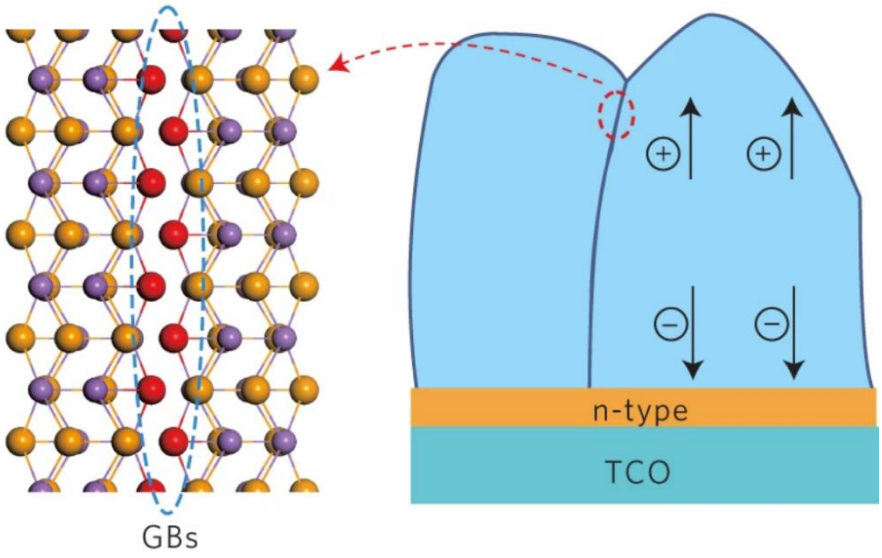

Figure 11: Columnar structure of Sb_2Se_3 (left) and grains (right) [14].

2.3.3 Metal chalcohalides

Introducing a halide to a chalcogenide creates a chalcohalide. For instance, the iodination of Sb_2Se_3 creates SbSeI. The same can be done using bromine (Br) by bromination of Sb_2Se_3 creating SbSeBr. According to [15], these materials show a theoretical wide bandgap, making them more interesting for semi-transparent applications. This also makes them a good potential top cell for tandem devices. Limited research has been done on these materials [15].

Appendix B states that just like chalcogenides these materials also have a quasi-1D structure of the crystals. However, the full advantages of the chalcohalides have yet to be unlocked. One of the main challenges is the perpendicular orientation of the structures with respect to the sub-/superstrate. The smooth thin-film morphology of the material also needs to be optimized. To realize the valuable properties much research needs to be done to understand how the material behaves under specific synthesis conditions and techniques.

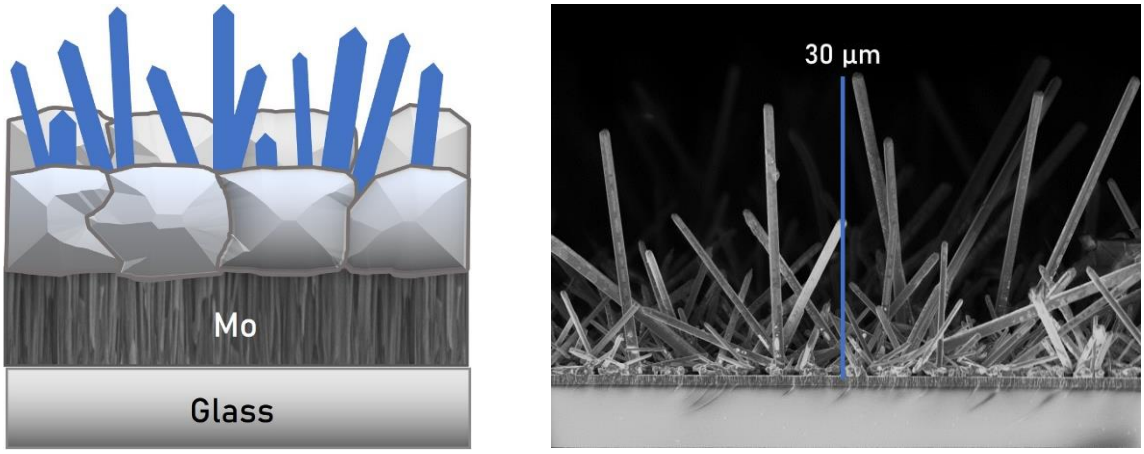

Figure 12: Cross section of SbSeI deposition showing non-parallel columnar structures (see appendix B).

2.4 Conclusion

A good carrier selectivity and transport are a big performance factors in a solar cell. So, it is important to investigate is the compatibility or in other words a good bandgap alignment with different selective contacts. These materials must be matched with compatible layers to successfully extract carriers to the front- and back contact. Many configurations are possible, and each will have a different result depending on layer compatibility, good physical coverage and suitable morphology with every layer deposition.

3 Experimental procedures

3.1 Workplan

The general objective of this thesis is to investigate the best suited device architecture and electrons/holes selective contacts for emerging thin film Van der Waals PV technologies based on SbSeI and SbSeBr mixed chalcohalide compounds (see appendix A). This is achieved through the synthesis of different device configurations with predetermined materials and their already developed deposition technique at UPC. In parallel, Sb_2Se_3 devices are synthesized as reference devices to compare possible performances. The synthesis roadmap is visible in appendix A.

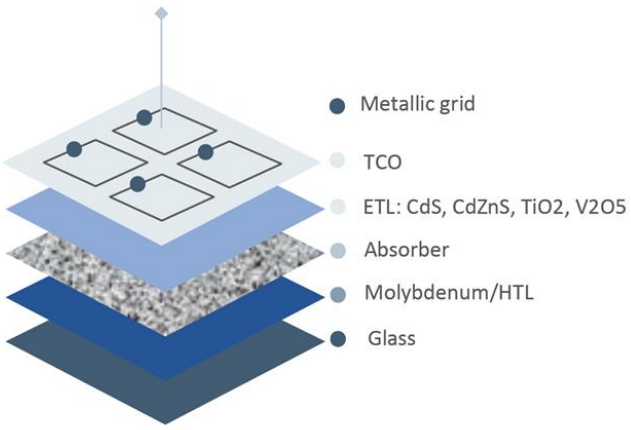

Figure 13: Different layers for substrate configuration devices (see appendix A).

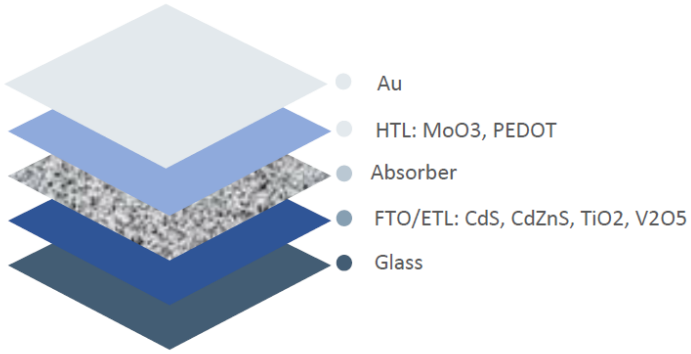

Figure 14: Different layers for superstrate configuration devices (see appendix A).

3.2 Synthesis plan

A synthesis plan of all the different device configurations is made to minimize equipment time, material usage and assistance. Laying out all the devices that must be made also paints a clear picture about workload and planning of all deposition processes, especially when equipment is only available on other locations. Due to optimization issues with the SbSeBr absorber, the decision is made to focus on SbSeI instead. The superstrate configuration devices that are planned with an SbSeBr absorber are changed to the Sb_2Se_3 absorber and will function as reference devices. This will hopefully shed light on performance and other differences in device characteristics. A total of 18 devices are planned.

Figure 15: Original synthesis plan of all planned devices.

3.3 Synthesis of devices

3.3.1 Chemical vapor deposition (CVD)

Thin films can be synthesized by CBD. By using a precursor, a reaction takes place on the substrate to produce a desired layer. At the PV-group the main CVD techniques is co-evaporation and atomic layer deposition (ALD).

Co-evaporator for Sb_2Se_3 deposition

According to [16], the thermal evaporation principle is based on heating and evaporating a material. Increasing temperature increases the vapor pressure of the material until a vapor is formed. The vapor will be deposited on the rotating substrate. The complete process is done in a high vacuum to reduce interaction from vapor particles with any impurity in the atmosphere resulting in a more even and controlled film deposition [16].

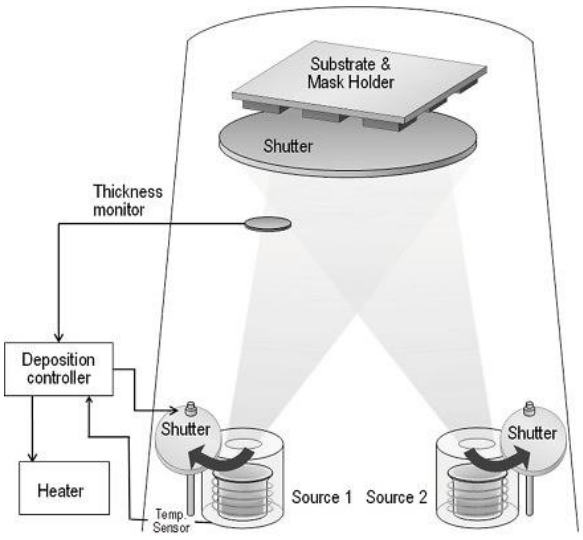

Figure 16: Thermal evaporation principle [17].

The PV-group at UPC has such equipment in the PVD-lab and is called the Kenosistec co-evaporator. Which is one part of a two-function machine that has two has two high vacuum (up to 10^{-8} mbar) chambers. One for sputtering and one for co-evaporation, both are connected via a third chamber with a robotic arm that inserts or removes samples without the need to open the chambers. The co-evaporation system is fully automatic, and a wide variety of parameters can be programmed to create the perfect deposition recipe for corresponding materials. Figure 17 shows the open chamber of the co-evaporator with the sample holder on the top and four effusion cells on the bottom. Each effusion cell can radiatively heat up a crucible with a corresponding material to temperatures up to 700°C. Cells can be closed by a shutter to either start or stop the deposition. The main use of this chamber is the deposition of Sb_2Se_3 and Bi_2Se_3. Depending on which crucible contains a specific material, the right recipe is selected with optimal deposition- temperatures, vacuum pressure and time. For Sb_2Se_3 the co-evaporation recipe is optimized for a deposition thickness of 800nm.

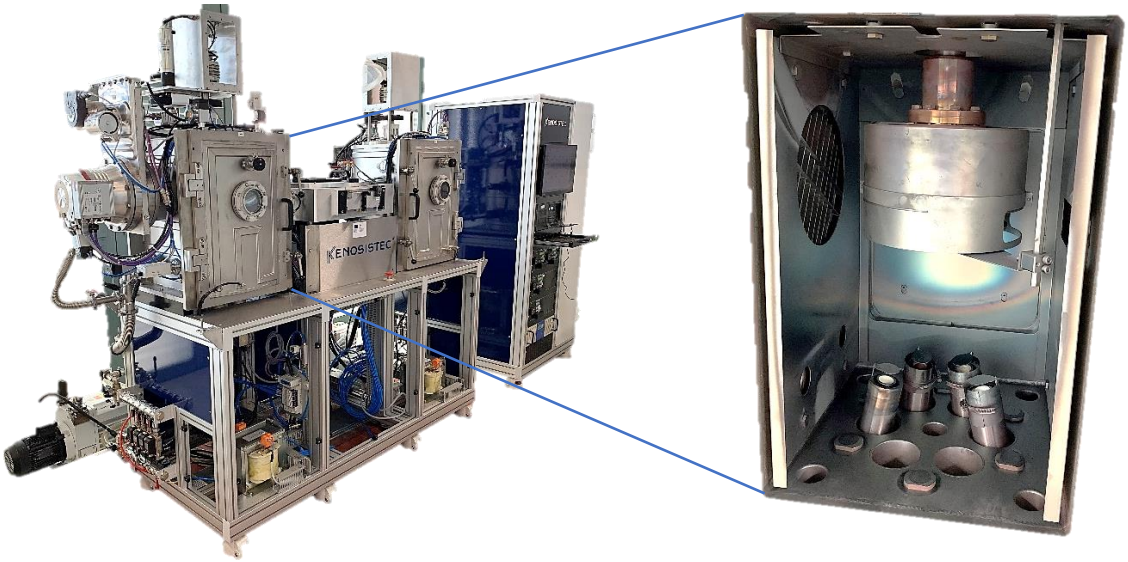

Figure 17: Kenosistec system (left) and the open co-evaporation chamber (right).

Atomic layer deposition for TiO_2 and V_2O_5

[18] states that ALD is a sequential chemical process that occurs in a reactor using different precursors. This is achieved at a certain temperature and vacuum pressure. This deposition technique has the advantage of having a conformal and reproducible thickness that is linear to the number of cycles. When depositing TiO_2, two precursors are used: $TiCl_4$ and H_2O. By exposing the samples to $TiCl_4$, it will react with the substrate surface creating a first layer. The second step will introduce the H_2O precursor and react with the $TiCl_x$ and replace the Cl with oxygen (O) to form TiO_2. These two steps are considered to be one cycle, which creates one layer of TiO_2. A total of 25 cycles are done with every sample, this results in a TiO_2 of 2nm. The same principle is used for V_2O_5 and a total of 200 cycles are done at 150°C, resulting in a thickness of 10nm.

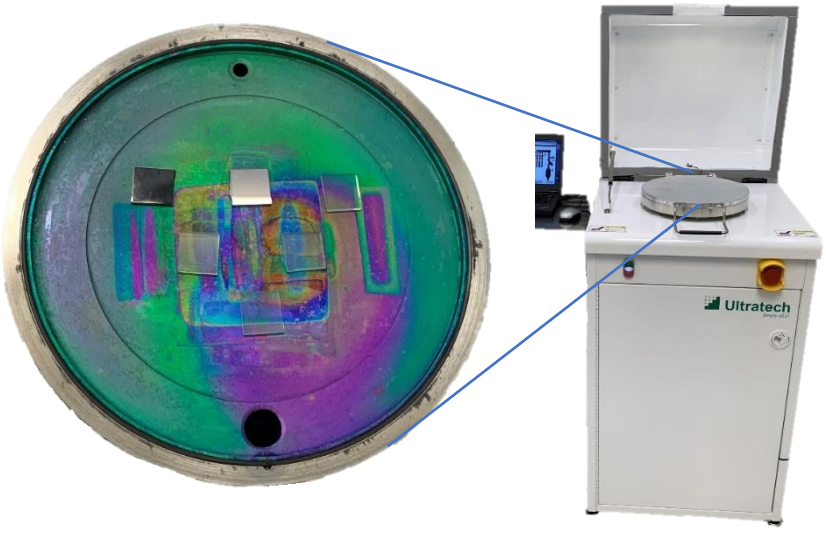

Figure 18: An Opened ALD reaction chamber with samples (left) and a complete ALD system (right).

3.3.2 Physical vapor deposition (PVD)

PVD is mainly focused on thermodynamic, mechanical and electromechanical types of deposition. The PVD-lab contains a number of equipment for deposition of thin films such as: a co-evaporation system, a sputtering system and a thermal evaporation system inside a glovebox [19].

Thermal evaporator for Ag and MoO_3 deposition

The PVD-lab is also equipped with a thermal evaporation system which works on the same principle as the co-evaporator. This evaporator, however, is inside a glove-box in a nitrogen environment. It uses a boat between two electrons to create a high temperature. Materials are introduced inside a tantalum (Ta) boat. For high temperature depositions a Tungsten (W) boats are used. Before deposition, the evaporator hood covers the system and vacuum pumps extract nitrogen until high vacuum (up to 10^{-6} mbar) is reached. Unlike the co-evaporator, the thermal evaporator needs manual adjustment of the power to the electrodes to control deposition rate. This rate is checked via a quartz crystal microbalance (QCM) also called a thickness monitor [20]. depending on the desired rate offset, the power is adjusted. For the planned devices this equipment will mainly be used for the deposition of an Ag and Au metallic grid for electron extraction. The desired deposition thickness for this layer is about 500nm and is deposited at a rate of 5Å/s (= 0.5nm/s).

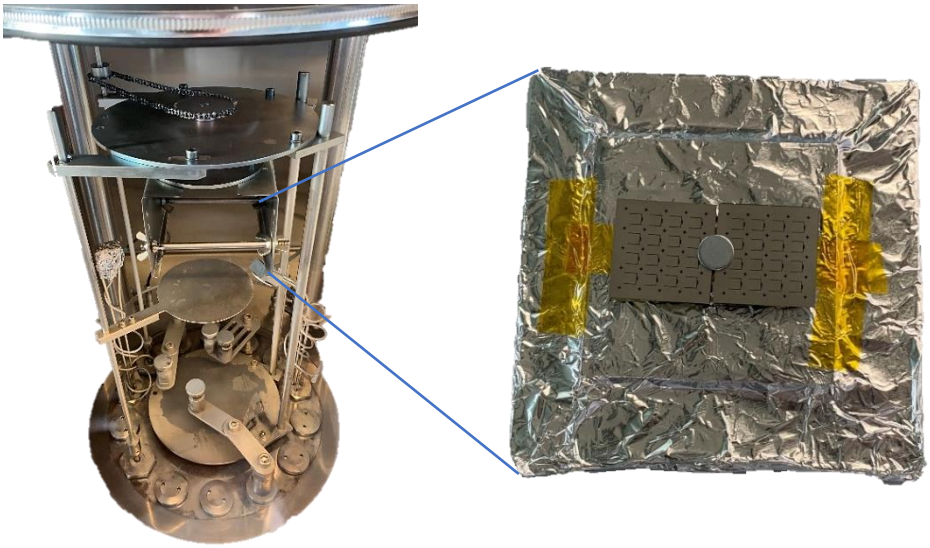

Figure 19: Thermal evaporation system inside a glovebox (left) and sample holder with grid masks (right).

Regarding the thermal evaporation of MoO_3, optimum selectivity has been found by the team at a thickness of 20nm. According to [20], the QCM is not always ideally positioned due to space constraints inside the chamber. This might result in a different deposition rate on the sensor compared to the rate on the substrate. Therefore, a correction factor or tooling factor of 0.8 is introduced to counter the offset. This means that to achieve a 20nm thickness, the deposition should only be stopped a measured thickness of 25nm.

Sputtering for Mo deposition

A second form of PVD is through sputtering. [21] states that this technique is quite sophisticated for depositing thin films but is one of the most used processes in the industry. Putting a voltage over a cathode and anode (= substrate holder) creates an electron flow to the cathode (= target). A magnetic field is introduced near the cathode to keep these electrons close to the target. This means a higher concentration of electrons is present near the target. By introducing a gas flux (argon etc.) into the vacuum chamber, there is a possibility of argon atoms colliding with electrons near the target. This collision results in free electrons and an ionized argon atom, visually seen as a plasma. If the geometry is correct, the ionized argon hits the target at immense speed and essentially ejects atoms from the target surface. This ejected material will travel in a straight line covering the complete chamber and the substrate in the process. Layer thickness and morphology are dependent on power and deposition time [21].

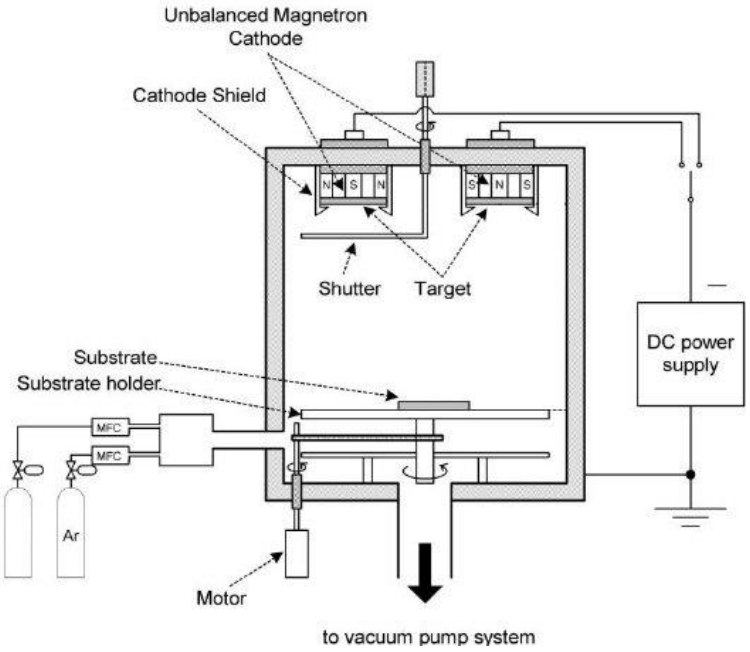

Figure 20: Sputtering principle [22, P.2].

For this project, the system will mainly be used for substrate configuration devices for the deposition of 800nm of Mo and ZnO/ITO with thicknesses of 50nm and 250nm respectively. Because of the process not yet being optimized at the PV-group, the deposition takes place at IREC. IREC is a public research institution that is accessible to students from the PV-group. The Mo deposition has been optimized there and shows exceptionally reliable and repeatable quality to form the first layer on SLG for substrate devices.

3.3.3 Chemical bath deposition (CBD) for CdS

[23] states that this method of depositing a thin film is used extensively in solar cell synthesis. It is used reliably, at low- cost and temperature. CBD is perfectly scalable in the industry with reproducible results. The CBD principle works by introducing samples/substrates in a heated aqueous solution of different chemicals that create a heterogeneous nucleation of CdS on the substrate surface. Since CdS is very toxic, the whole experiment is done in a fume hood and by using the right personal protection equipment.

At the PV-group, CdS deposition happens in the chemical lab, which has a dedicated fume hood for CdS deposition and etching treatments. The CBD setup exists of an ultrapure water bath with a beaker that contains 100ml of ultrapure water, 55ml of cadmium nitrite ($Cd(NO_3)_2$), 30ml of sodium citrate ($Na_3C_6H_5O_7$), 5ml of ammonia (NH_3) and 10ml of thiourea ($SC(NH_2)_2$). The beaker is stirred at a temperature of 75-80°C. Than a sample holder with Kapton tape holding the substrates is introduced and the beaker is covered with Aluminum. The process takes approx. 40min. After a while, the nucleation of CdS becomes visible by the yellow color of the solution.

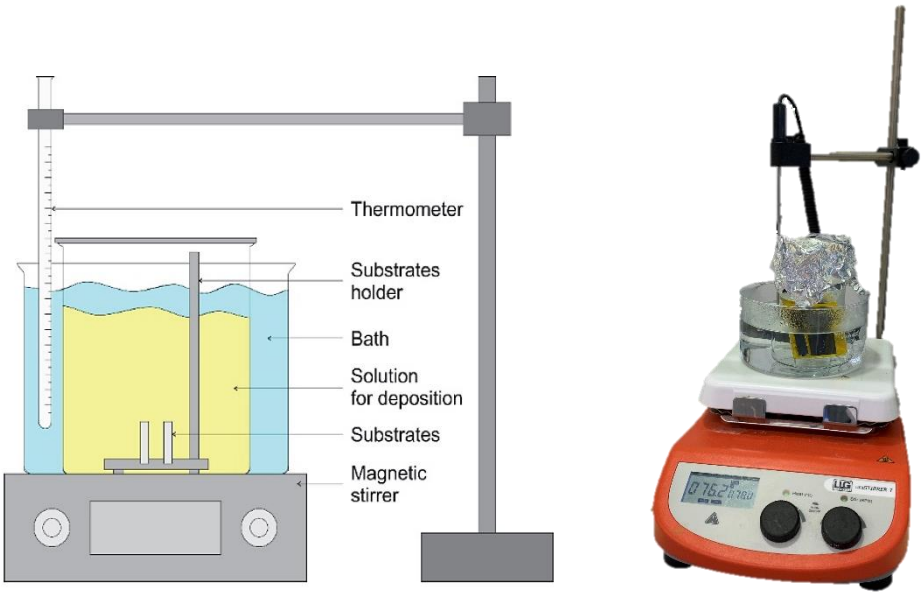

Figure 21: CdS CBD principle and CBD setup at the PV-group [24, p.13].

3.3.4 Low-pressure annealing for post-selenization

After depositing the Sb_2Se_3 absorber, a low-pressure annealing of the substrate is done. This is done in the thermal lab at the PV-group that contains a number of annealing furnaces for different temperatures and pressures. According to [14], depositing Sb_2Se_3 using evaporation, creates a thin-film with good absorber properties. However, by adding a post-selenization step to the deposition increased the overall fill factor (FF) and efficiency of the synthesized devices. At the PV-group this process is done in the thermal lab using a low-pressure furnace from Nabertherm.

Figure 22: Nabertherm low pressure furnace.

The basic principle is to introduce a Sb_2Se_3 sample and 2,5mg of selenium in a Petri dish. This Petri dish is than placed in the quartz tube of the Nabertherm furnace. Next, the tube is vented multiple times to vacuum and refilled with Ar with a lower-than-atmosphere pressure, in this case the optimum was found at 335mbar at room temperature. It is important to have a lower pressure due to the gas expansion at higher temperature, the tube is not built for pressures above 1 atm. The last step is to close the furnace and select the program, the main parameters of the program are the time and temperature setpoints. The standard process is a ramp of 10°C/min to 320°C and stay at this temperature for 15 min.

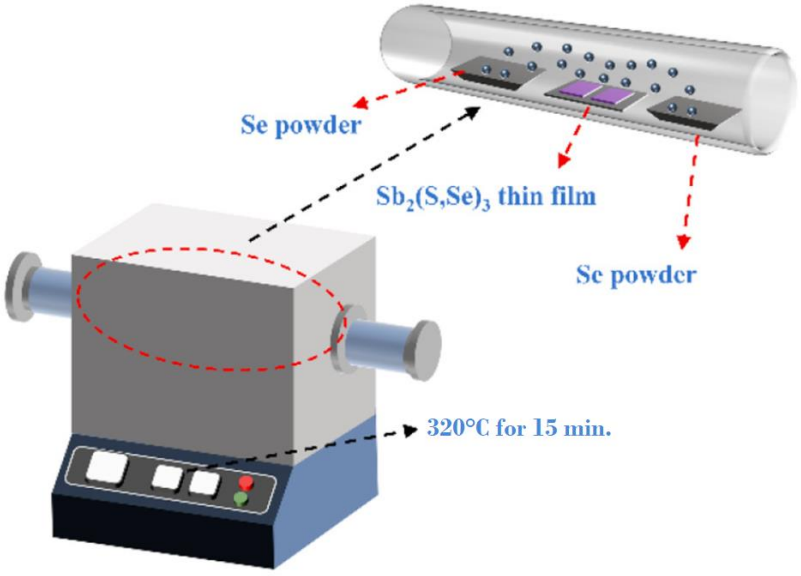

Figure 23: post-selenization principle [25].

3.3.5 High pressure high pressure annealing for iodination

According to appendix B, the formation of SbSeI comes from the complete reaction of Antimony triiodide (SbI_3) with a Sb_2Se_3 precursor. Presenting these two molecules in a high pressure, high temperature environment will force them to react and form SbSeI crystals. These crystals have the tendency to grow into columnar structures or ribbons that have strong bonding parallel to the ribbons. In the perpendicular direction, there is a small force present due to the van der Waals interaction.

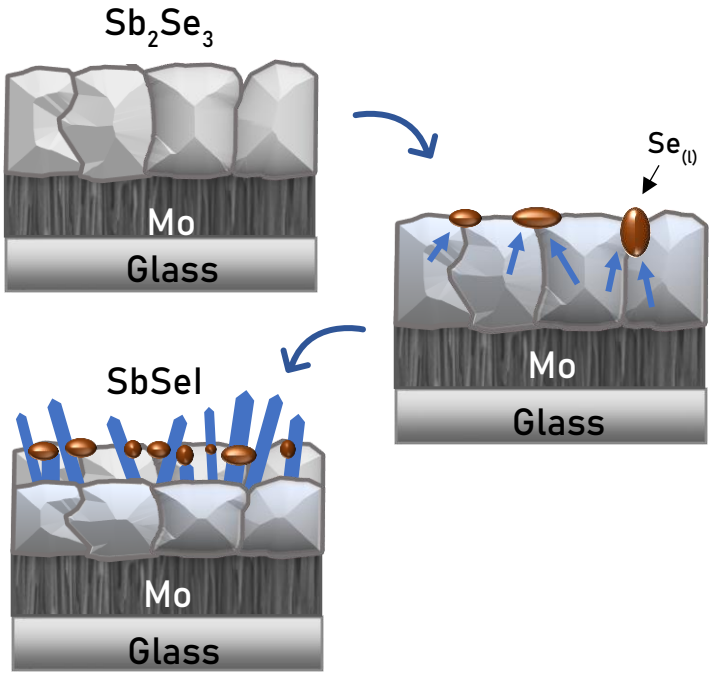

Figure 24: SbSeI formation principle (see Appendix B).

In order to synthesize SbSeI and grow the columnar structures, a precursor layer of Sb_2Se_3 is deposited on the sample using the co-evaporator. Next, the sample is introduced in a Petri dish together with 10mg of Se and 15mg of SbI_3 (see fig. 23). This is than introduced into the High-pressure furnace tube and sealed using bolts and nuts and a copper washer. Initial Argon pressure is set at 0.2 MPa (= 2 bar). Last, the PID setpoints are set to 450°C in 45min (= 10°C/min) and remain at 450°C for 15min. The complete process is done in the thermal lab using the MTI high pressure furnace.

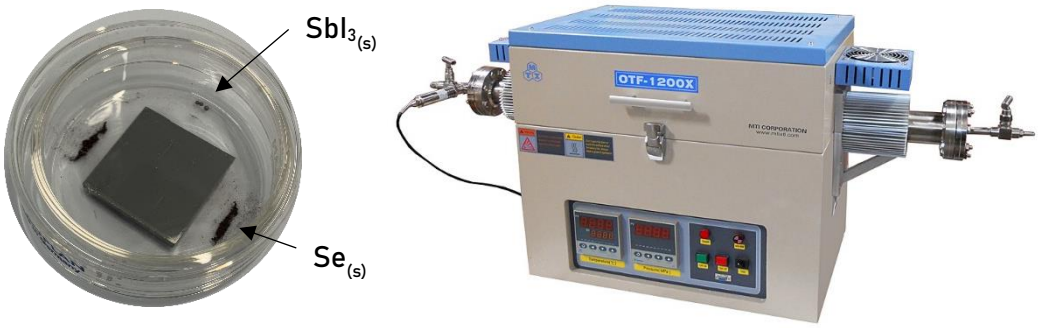

Figure 25: Prepared Petri dish (left) and the MTI High pressure furnace (right) [26].

3.3.6 Spin coating of PEDOT:PSS

According to [27], thin films can be deposited by drop casting a low-viscosity solvent and rotating the sample at high speeds. This is the basic principle of spin coating. Rotation per minute (rpm) are usually between 1000 and 10 000. When a low viscosity solvent is applied on the sample, the centrifugal force will force the solvent off the sample and leave behind a thin film. The thickness of the film depends on the rpm and viscosity of the solvent. Low rpm and/or high viscosity will result in a higher thickness film on the sample, while a high rpm and/or low viscosity results in a lower film thickness [27].

At the PV-group this is done using a SPS Polos spin coater inside a nitrogen filled glovebox. The sample holder is made from leftover SLG and Kapton tape to make sure the samples are held firmly during the rotation. This holder is than introduced on the suction pad of the spin coater. To make sure the holder itself does not loosen during the process, vacuum pressure is achieved between the holder and the suction pad. Next, about 12 drops of poly(3,4-ethylenedioxythiophene) polystyrene sulfonate (PEDOT:PSS) (HTL solar) are introduced on the sample surface [28]. The lid is than closed and the spinning cycle consists of a 500rpm/s increase to 1000rpm for a total of 60s. Last, the sample is removed and annealed on a hot surface of 115°C for 15min. This complete process results in a conform layer of PEDOT onto the sample.

Figure 26: PEDOT solvent (top left), sample holder (middle) and spin coater (right).

3.3.7 Diamond point scribing and indium (In) soldering

Once all the layers are deposited on the substrate, every cell needs to be electrically isolated. This is realized using a scribing equipment at IREC. The scribing equipment consists of a precisely positioned diamond point that scratches through all thin film layer except for Mo and FRO, which are the back and front contact respectively. This creates smaller sub cells of 5x5mm.

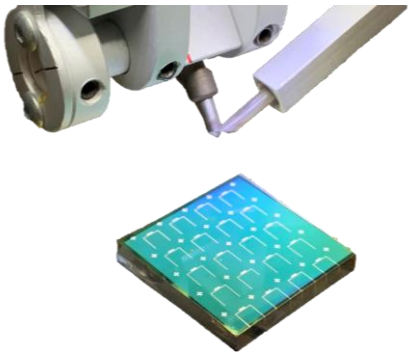

Figure 27: Diamond point and scribed device.

A last step of the synthesis process is indium soldering. Indium is used as a practical connection to the underlying front or back contact of devices, which select and extract generated carriers. Indium is a softer material that allows for a better connection with the contacts and measurement probes (see fig. 28). For substrate devices, the top layers are scratched off in the corner of the device until the Mo (back contact) is reached. This creates a small area for indium to be soldered on. This process is similar for superstrate devices and also requires the scratching of the top layers until FTO (front contact) is reached. Indium is than soldered on the FTO (see fig. 28).

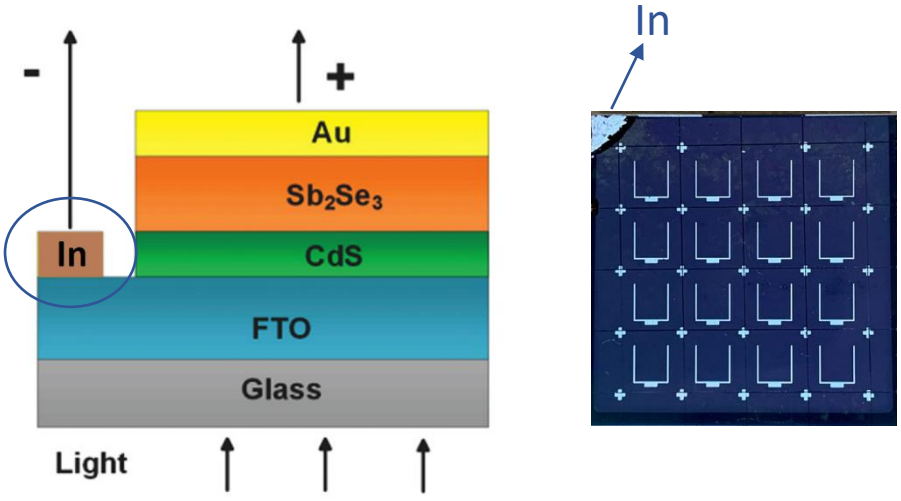

Figure 28: Indium solder on FTO for superstrate devices (left) and In solder on the Mo for substrate devices (right) [14, P.6].

3.4 Characterization

[29] states that multiple characterization techniques are used to analyze and assess performance of finished devices. Ranging from visual to optoelectrical analysis. Characterization is complex due to the many variables for each technique such as illumination, wavelength, temperature, etc.

3.4.1 Solar simulator

According to [29], the Shockley-Queisser (SQ) limit is based upon certain assumptions:

1. Absorption of all photons with $E_{photon} >= E_g$ of the AM1.5 solar spectrum.
2. Collection of all generated carriers at the contacts.
3. Thermalization of all carriers to band edges.
4. No collection losses besides radiative recombination.

The following topics are explained with the SQ limit in mind. Solar simulation is used for optoelectrical analysis of devices, specifically the JV-curve response upon illumination with the solar radiation spectrum (see fig. 29) on the earth's surface also known as AM1.5. Because of the nature of this spectrum, there is a fixed photon flux pattern (see fig. 29). The lower the bandgap of a material, the higher the number of generated electrons due to more photons with $E \geq E_g$. So, the lower the bandgap, the higher the current density [29].

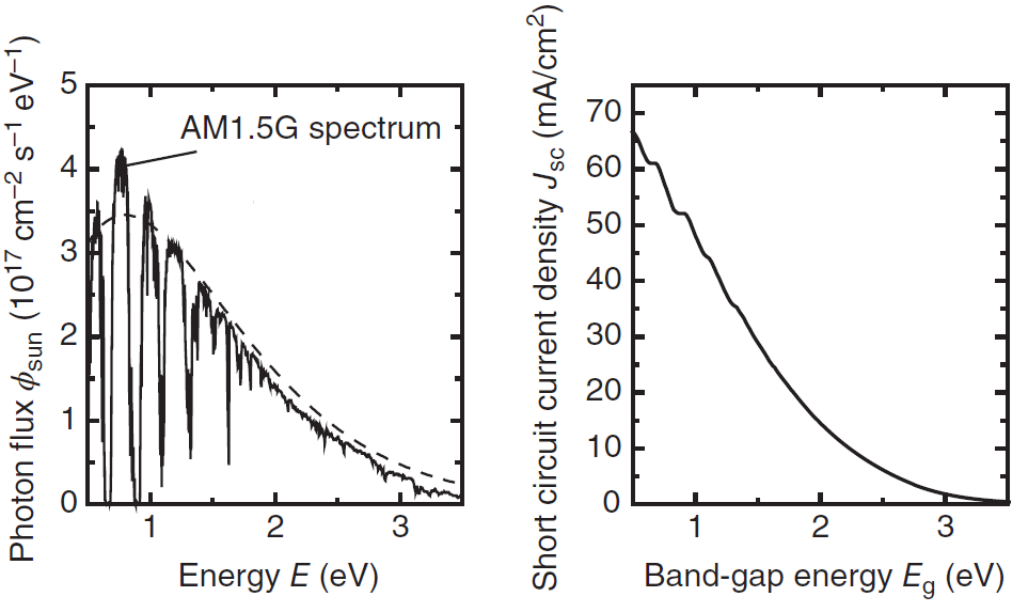

Figure 29: Solar photon flux on earth's surface (left) and corresponding bandgap energies (right) [29, P.7].

However, according to [29], this would mean a decrease in V_{oc} which influences the total power output. So, a balance between these two parameters is important to optimize power output of a device. An optimum and thus maximum efficiency for single junction devices is found at 33% (see fig. 30). By combining other wide bandgap materials higher photon absorption and thus higher efficiencies are possible. Since the innovative materials such as Sb_2Se_3 and SbSeI have a wider band gap and semitransparent properties, they make an ideal candidate as a top cell in combined with Si in a tandem cell configuration.

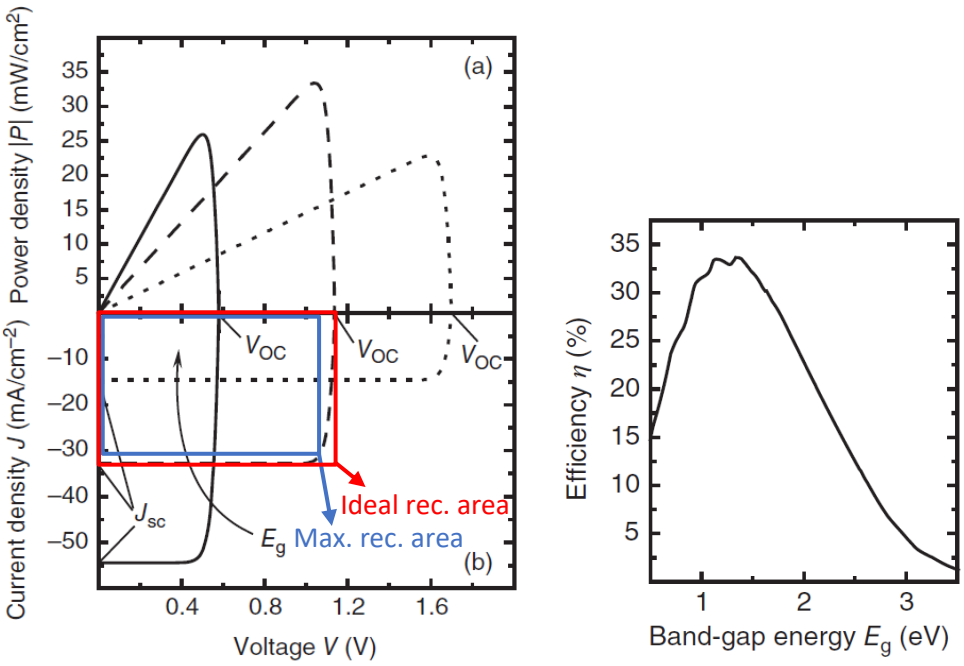

Figure 30: JV-curve and power density for bandgap energies E_g= 0,8; 1,4 and 2,0 eV (left) and the conversion efficiency in function of E_g in the SQ limit [29, P.8,9].

Good carrier collection is indicated by a good fill factor (FF). Which is the highest possible rectangle surface area (see blue square, fig. 28) below the JV-curve divided by the ideal solar cell surface area (see red square, fig. 28). Whenever high recombination or low carrier mobility occurs, due to interfaces or defects, a more S-shaped JV-curve is visible. This leads to a lower rectangle surface area and thus lower FF [29].

At the PV-group, Sb_2Se_3 and SbSeI devices are tested using a Pico solar simulator from G2V Optics, which has light emitting diodes (LED) to simulate the AM1.5 solar spectrum (see fig. 31). Probes are used to connect the back and front contact to the measurement hardware. The measurements are registered and plotted on a software package 'IV-Characteristic' [30]. Every sub cell is given a name and tested in a voltage range of -200mv to 600mv in 150 steps and a compliance current of 100mA, a last parameter is the surface area of each sub cell which for these devices is 0,25cm^2. The test starts by selecting 'Calculate the PV parameters'. After a certain period, the JV-curve is plotted and saved in .xlsx format. Measurement results include J_{sc}, V_{oc}, FF and Efficiency. Efficiency is calculated using the following formula: $Eff = \frac{(V_{oc} * J_{sc} * FF)}{P_{incident}}$, $P_{incident}$ being the power by the solar spectrum incident on the cell surface. This data is than imported and treated in a software package OriginPro.

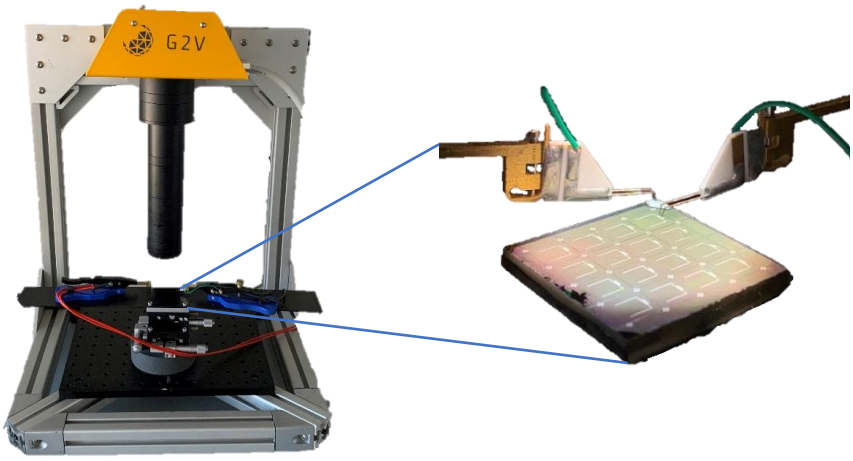

Figure 31: G2V Optics Pico (left) and sample SUB-1 connected to the probes (right).

The probes of the solar simulator are connected to a regulated resistive load, which changes throughout the measurement. V_{oc} is measured by simulating an open circuit, this is done by connecting an 'infinite' resistive load. J_{sc} is measured at short circuit, this is done by disconnecting the load, meaning that the resistivity is 'zero'.

3.4.2 Scanning electron microscopy (SEM)

A first technique for characterizing devices is SEM. This is a visual type of characterization to analyze surface morphology and cross-sectional layouts. According to [29], the wavelength of visible light limits the resolution in an optical microscope. Therefore, SEM uses electrons which have a shorter wavelength and allow for a higher resolution imaging. An electron gun is used as an electron source, the electrons than travels through a variety of electromechanical lenses to focus the electron beam onto a small area and hit the sample (see fig. 32). The atoms on the surface emit secondary electrons, which are than seen by a detector. Imaging is done by introducing a sample in the SEM chamber. This chamber is kept at high vacuum to prevent electrons from scattering due to gas molecules [29].

An important part of SEM imaging is the prevention of sample charging. This happens when electrons build up in the sample and less electrons are emitted and detected resulting in a lower quality image. To prevent this from happening samples should be conductive or coated (by sputtering) with Au or carbon (C) layer.

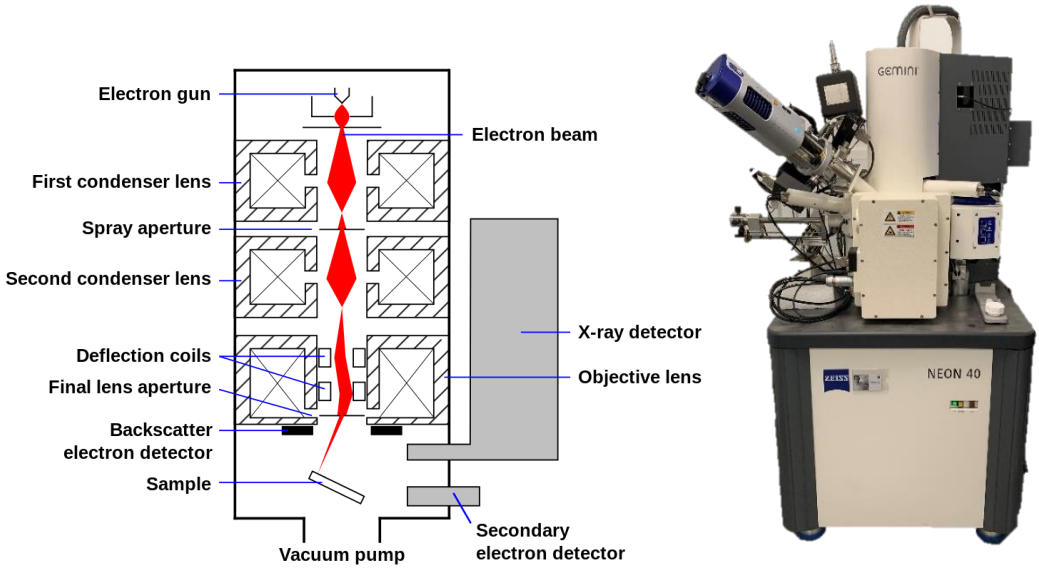

Figure 32: SEM principle (left) and the SEM at UPC (right) [29].

3.4.3 External quantum efficiency (EQE)

[29] states that EQE is equal to the total collected electrons at the contact for the total incident photons that were exposed to the sample. Using the SQ limit, representing the ideal situation, EQE = 1 for $E_{photon} \geq E_g$. In the real world, this is not the case, and EQE < 1 for $E_{photon} \geq E_g$ due to losses occurring in the process. These losses come from reflection, recombination losses and parasitic absorption of photons in layers that will not result in electron-hole pairs over the junction (see fig. 33).

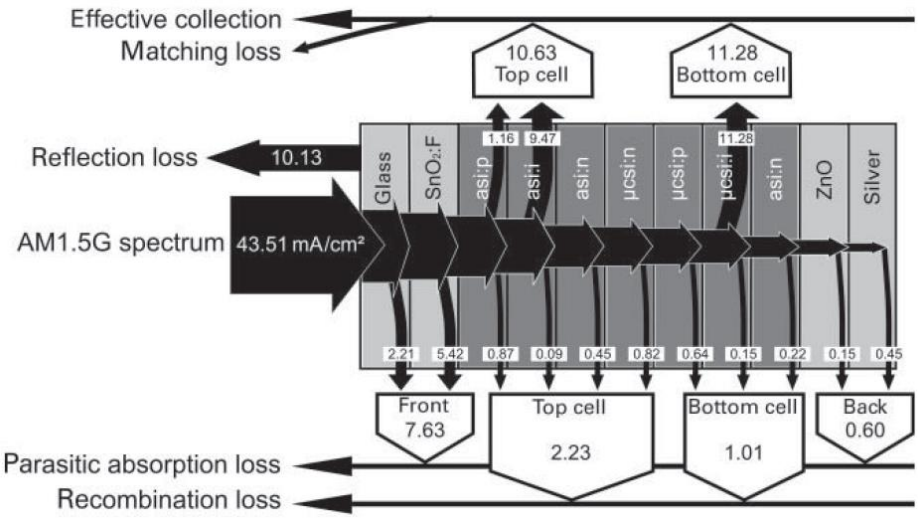

Figure 33: Example of losses in a tandem device [29, P.65].

At the PV-group EQE measurements are done using a monochromator at IREC (see fig. 34.). According to [29], the principle of a practical EQE measurement is exposing the sample to one wavelength or in other words monochromatic light. This step is repeated for a spectrum of wavelengths and the J_{sc} is measured for every wavelength and the number of photons emitted onto the sample. With these two parameters the EQE is plotted. The setup consists of a xenon (Xe) light source exposed to the monochromator, inside the monochromator the light is diffracted using a series of mirrors until a single wavelength is filtered out and exposed to the sample and monitor cell (see fig. 34).

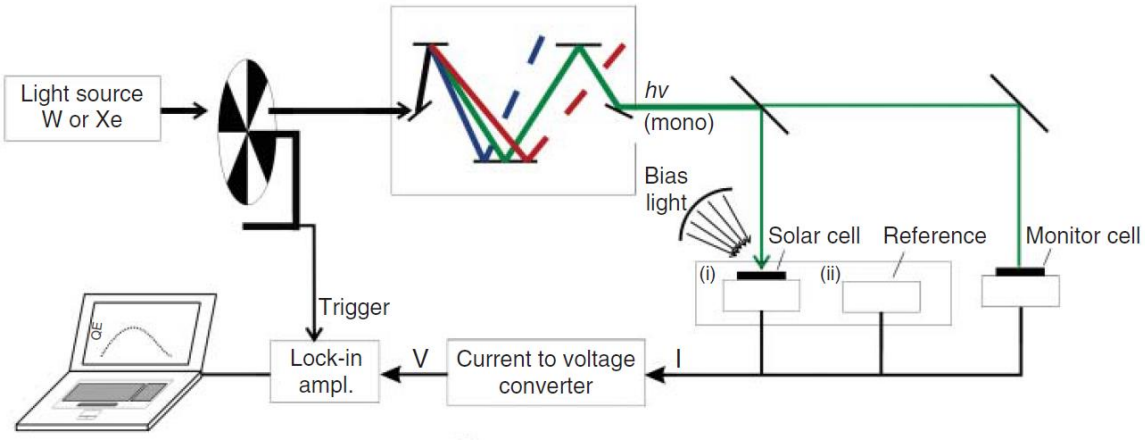

Figure 34: EQE measurement equipment using a monochromator [29, P.57].

[29] states that it is possible to roughly identify the absorption in each layer for the different EQE conditions. Wavelength in a way, corresponds with the penetration depth of the photons. Some of the incoming light is reflected, not contributing to current generation, this can happen at the interface of every layer and thus reflection contributes to a lower EQE throughout the thin film. First, light enters the window layer. Due to the bandgap of these materials, a portion of the photons with $E > E_{window}$ will generate electrons-hole pairs. This creates holes that are 'trapped' close to the ETL, being the CdS selective contact, and will contribute to recombination with electrons coming from the ETL and absorber region. In the ETL region photons with $E > E_{ETL}$ will also generate electron-hole pairs, but due to diffusion and the influence of the space charge region some of the carriers will drift in the right direction, contributing to the current generation, hence the increase of the EQE when wavelengths come closer to that of the absorber. In the absorber region the highest EQE is present. This is due to the large electron-hole generation contributing to the electron current. Due to the presence of the space charge, carriers easily drift toward the selective contact. The declining EQE in the bulk of the absorber is due to the generation of electrons that exceed the collection length. Collection length L_c is the distance that a generated electron can diffuse to, plus the drifting distance of a carrier due to the space charge region. Closer to the back contact, the distance of generated electrons becomes physically to far to reach the front contact. So with increasing wavelength and further penetration towards the back contact, generated electrons are less likely to make it to the front contact and will not contribute to current, decreasing the EQE. Another contributor to a decreasing EQE in this region is the non-absorption of photons. This can be caused if the absorber is too thin where a photon with sufficient E is not absorbed. The probability of non-absorption increases with longer wavelengths [29].

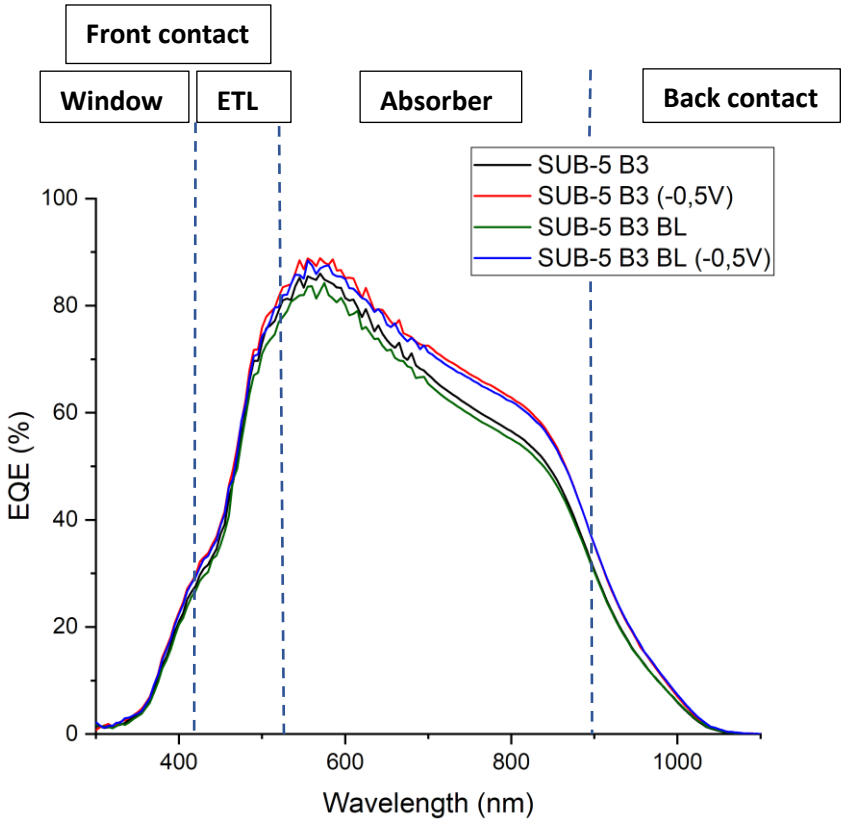

Figure 35: Example of EQE measurement.

3.4.4 X-ray diffraction (XRD)

XRD is a measurement technique to analyze crystal structures in samples. According to [29], the reason for this measurement is to determine if the synthesis/deposition processes created the desired crystallinity. A bad crystallinity might indicate the presence of impurities or unreacted material. There are different techniques to do this type of measurement, for these samples the focus will be on θ–2θ diffraction. This is done using an X-ray source is exposed to the structures of the sample. The incident X-ray hits the sample at a certain angle θ, exciting electrons which in turn scatter incoming X-rays that can be registered by a detector. This is done for different values of θ. In practical terms this means the X-ray source and detector also change in position symmetrically and keep the scattering vector perpendicular to the sample surface (see fig. 35) [29].

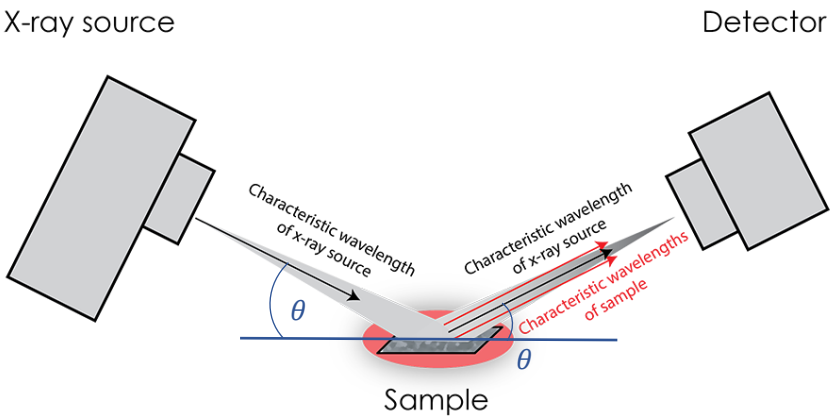

Figure 36: XRD setup of the source and detector [31].

According to [29], since the wavelength of an X-ray is similar to the space between atoms, they can travel in between crystal structures and penetrate inside the sample. As mentioned before, these X-rays will hit an electron and excite it, resulting in elastic scatting or the emission of the same X-rays in all directions. At specific angles, a constructive interference of the X-rays from other electrons in the structure, meaning that the emitted X-ray wavelengths are in phase. Similarly destructive interference is possible when X-ray is shifted ½ wavelength. When constructive interferences are seen by the detector, peaks are observed meaning that the second incident and the second reflected ray travel a multiple of the wavelength (=λ) further than the first ray. Eventually the measurement shows a graph of ray intensity in function of angle θ relating to the structure of the sample. This can than be compared to already known material graphs that are used as 'fingerprints'.

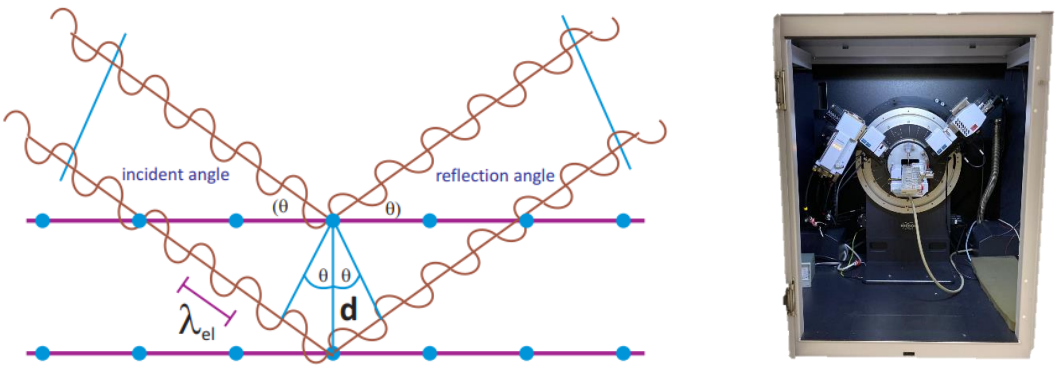

Figure 37: Constructive interference (left) and Bruker D8 Advance diffractometer (right) [32].

4 Results and discussion

4.1 Optoelectronic measurements

4.1.1 Efficiency

In this section, we explore the photovoltaic performance of 18 different device structures. A combinatorial approach is used with the aim of investigating the performance of 2 different absorbers (Sb_2Se_3/SbSeI) with three different ETL (CdS, TiO_2 and V_2O_5) in the substrate configuration. For this, the back contact ($MoSe_2$/Mo) configuration remains unchanged giving a combination of 6 devices . Figure 37 shows efficiencies for all six substrate devices, samples are labeled from SUB-1 to SUB-6.

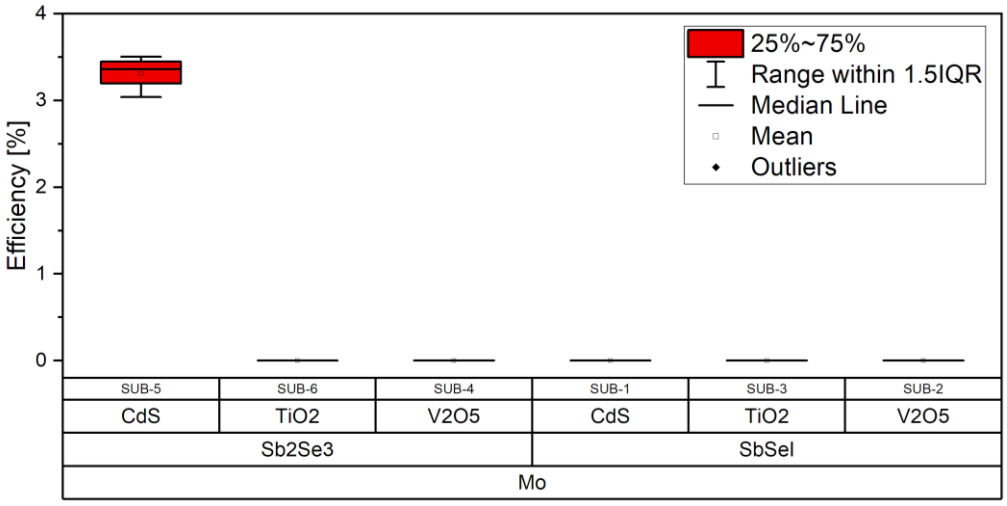

Figure 38: Substrate device efficiencies.

Figure 38 shows efficiencies for all twelve superstrate devices indicated by the 'SUPER' prefix. Describe the samples you are fabricating. Unfortunately, many devices are non-responsive, even the ones with Sb_2Se_3 as the reference material. Possible causes are discussed in further sections.

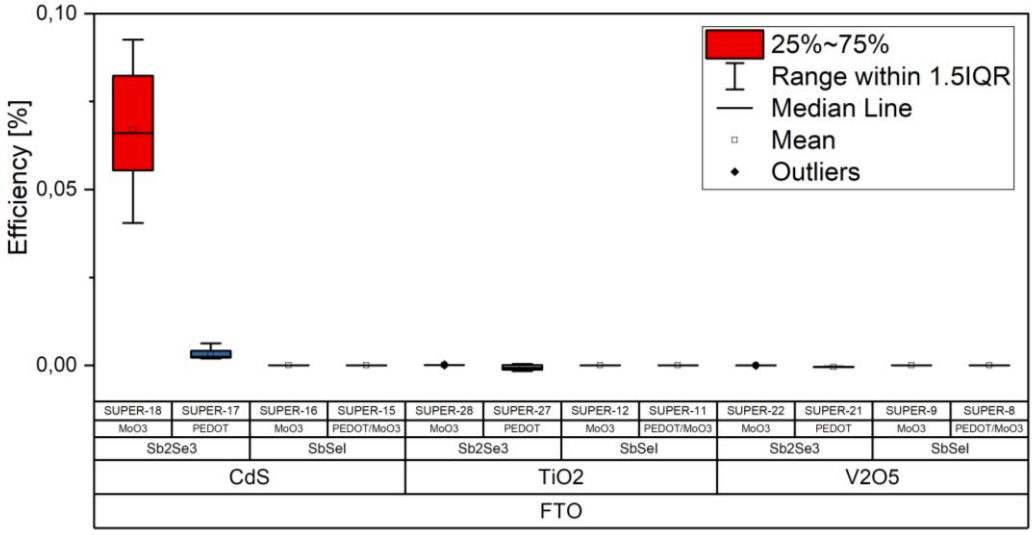

Figure 39: Superstrate device efficiencies.

4.1.2 Open-circuit voltage and short-circuit current

This section shows the V_{oc} and J_{sc} of the only two working devices SUB-5 and SUPER-18 consisting of the following device configuration: Mo/Sb_2Se_3/CdS/ITO and FTO/CdS/Sb_2Se_3/MoO_3 respectively. SUB-5 and SUB-18 show mean V_{oc} of 380mV and 113mV and a mean J_{sc} of 15mA/cm² and 2,3mA/cm² respectively.

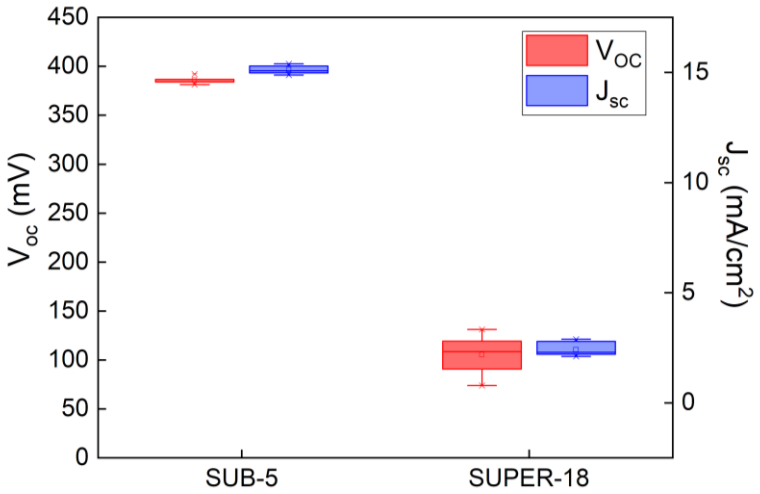

Figure 40: V_{oc} and J_{sc} of SUB-5 and SUPER-18.

4.1.3 Fill factor

As mentioned in 3.4.1, fill factor is calculated by dividing the maximum rectangular area below the JV-curve by the maximum rectangular area of the ideal JV-curve. The following plots show the efficiency and fill factor of SUB-5 and SUPER-18 with the mean FF equal to 56,3% and 24,1% respectively.

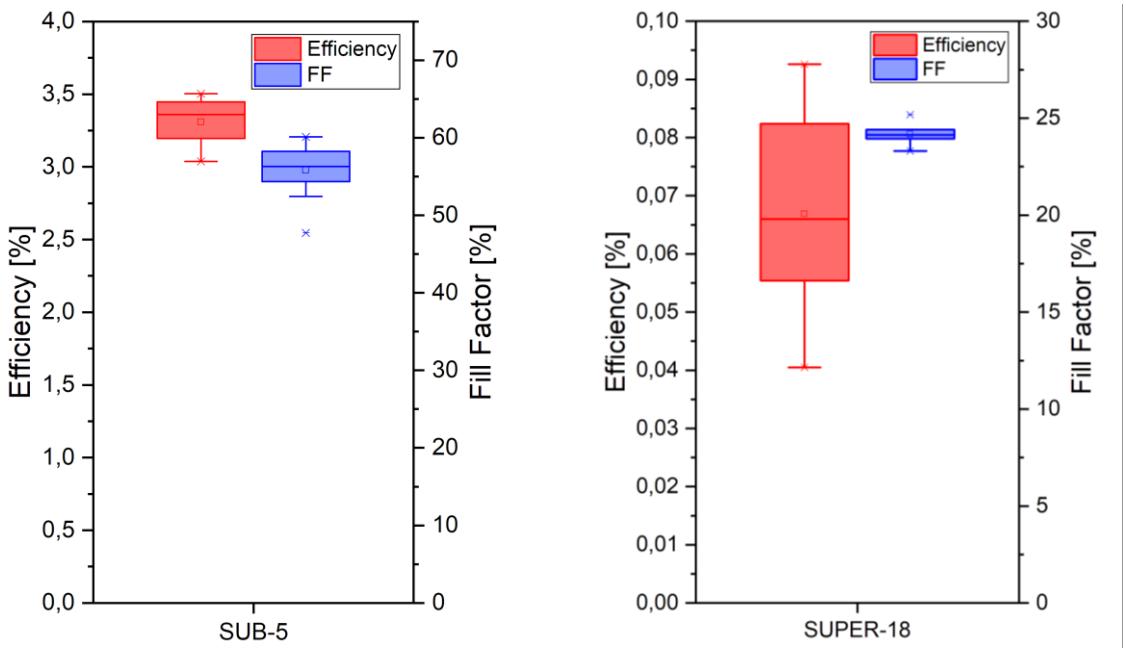

Figure 41: Efficiency and Fill factor of SUB-5 and SUPER-18.

4.1.4 External quantum efficiency

The following spectra show the EQE of sub cell B3 from device SUB-5 which consists of Mo/Sb_2Se_3/CdS/ITO. Sub cell B3 is measured in different conditions, ranging from monochromatic light, no bias voltage to bias light (BL) and a reverse bias voltage. EQE is measured for the following conditions:

Standard EQE 'SUB-5 B3': indicated by the green color, with EQE measurements for every wavelength by exposing the sub cell to monochromatic light.

'SUB-5 B3 (-0,5V)': indicated by the red color, represents the EQE with a reverse bias on the sub cell. A reverse bias essentially increases the space charge region width and facilitates minority carrier collection.

'SUB-5 B3 BL': indicated by the green color, represents the EQE by exposing the sub cell to 'white light' at the same time which might influence electron collection. Possible impacts will be discussed in further sections.

'SUB-5 B3 BL (-0,5V)': indicated by the blue color, represents the EQE by exposing the sub cell to 'white light'. As mentioned above, this might influence electron collection.

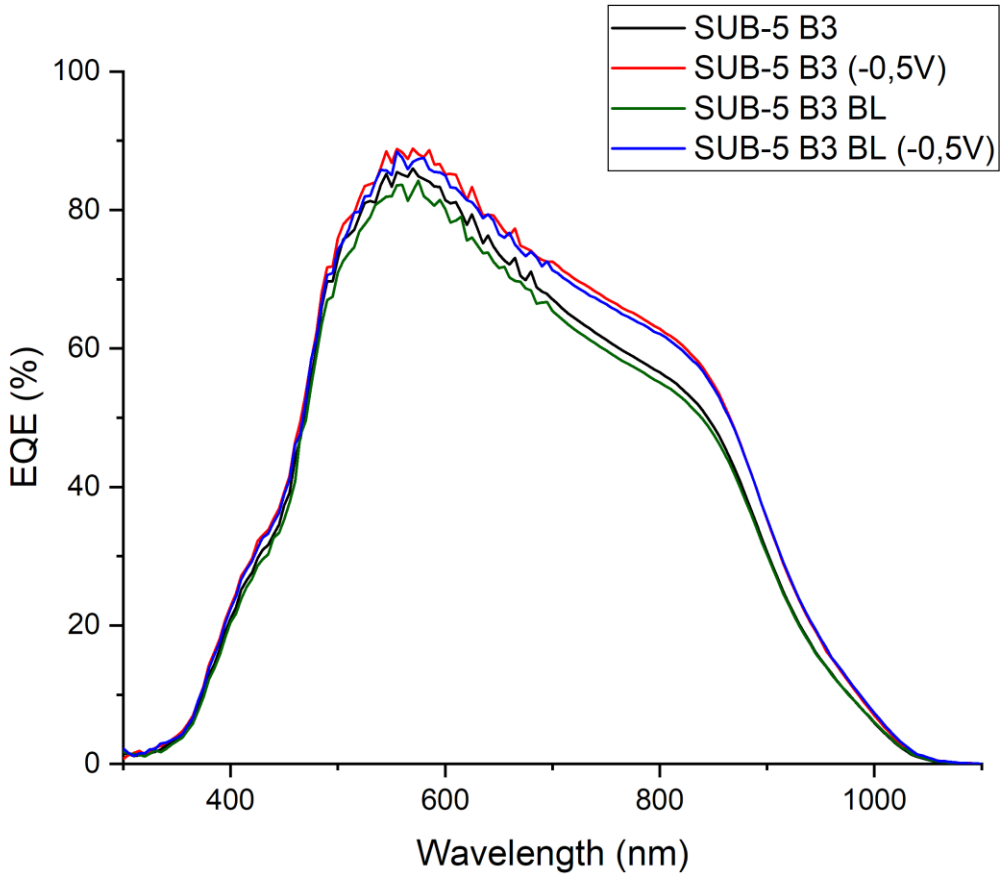

Figure 42: EQE plot of SUB-5.

4.1.5 Discussion

Efficiencies, fill factor, V_{oc} and J_{sc}

To minimize the effects of external factors and guarantee repeatability, devices are synthesized using same process parameters. Only two devices show a photovoltaic response. Of these two devices, SUB-5, which is the most optimized device structure in the group, shows the baseline efficiency, indicating that the quality of the absorber layer is not the limiting factor for the efficiency. SUPER-18 also shows a photovoltaic response with a rather low efficiency. Both of these devices are synthesized using the absorber Sb_2Se_3. The devices using SbSeI did not show a photovoltaic response.

SUB-5 has a configuration of Mo/Sb_2Se_3/CdS/ITO with good repeatability within the PV-group at UPC. Comparing this device to SUB-1 which has the same configuration but uses the metal chalcohalide SbSeI absorber. By comparing device SUB-1 to previously synthesized devices that also use SbSeI, a trend becomes visible. These devices were synthesized in a previous work at lower iodination temperatures (see Appendix C).

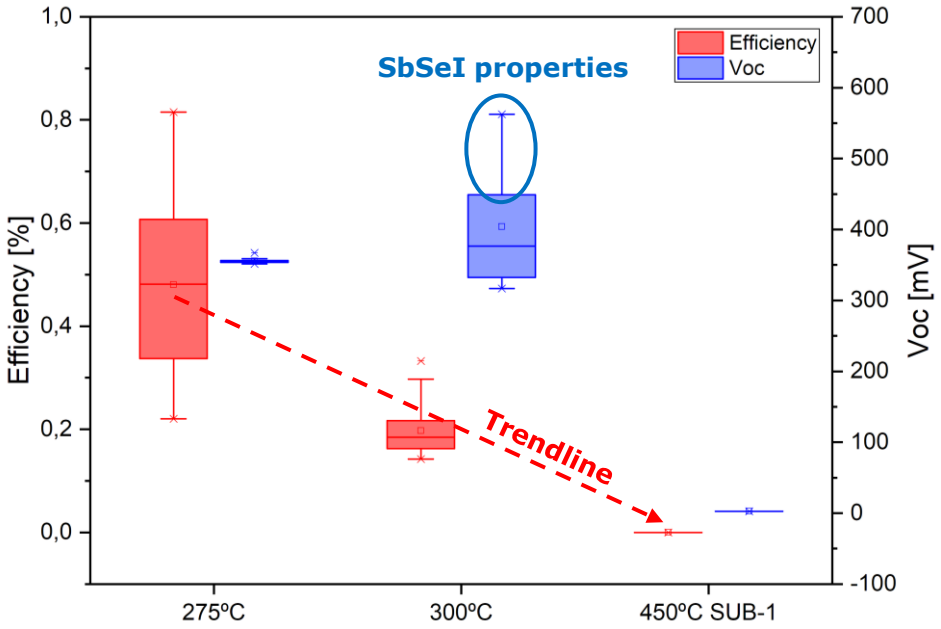

Figure 43: Comparing SUB-1 to previously synthesized devices at 2 bar and different iodination temperatures (see appendix C).

Important to note is that the devices synthesized at 275°C and 300°C shown in the figure above are fabricated using a different process for the precursor. The precursor is fabricated by depositing 250nm of Sb (by evaporation), next annealing the Se in a low pressure furnace, creating the Sb_2Se_3 precursor. As mentioned in 3.3.1, the precursor of device SUB-1 is synthesized using the co-evaporator, which evaporates both Sb and Se to create a Sb_2Se_3 precursor layer of about 800nm.

As shown in appendix C, by increasing iodination temperature, more precursor will react with the SbI_3 halide source. This means that at lower process temperatures, there is still unreacted precursor present (see fig. 43). It is believed that the Sb_2Se_3 precursor still being present in the lower process temperature devices, contributes to the efficiency and other optoelectrical features. This would mean that SUB-1 has a quasi fully reacted precursor with the halide source, creating SbSeI.

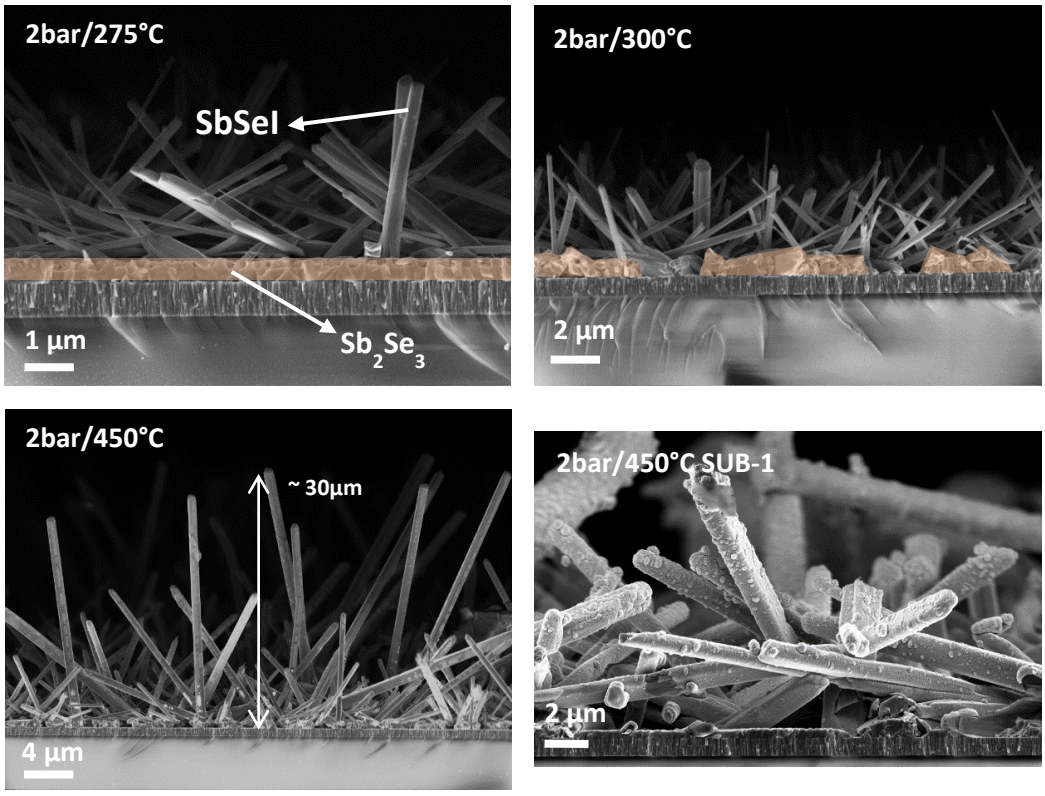

Figure 44: Cross sectional SEM images of devices at different iodination temperatures (see Appendix C).

Different assumptions are made about why SUB-1 shows non-responsiveness. Possibilities include a worsening coverage with increasing process temperature due to the formation of columnar structures or ribbons. According to Appendix B, this means that the underlying layer becomes exposed, in this case Mo. Upon deposition of the following layer, this might create shunt paths.

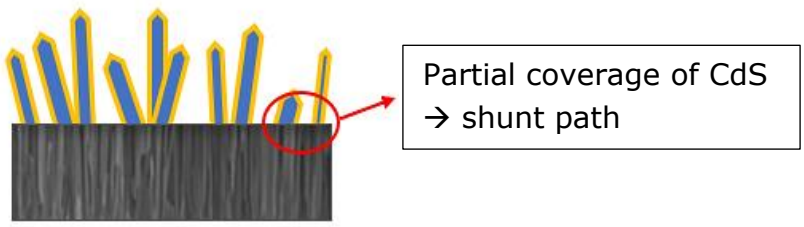

Figure 45: Formation of shunt path (see Appendix B).

Shunt paths might be solved by optimizing the iodination process. Trying to control ribbon height, orientation and coverage. An extension to this solution might be passivating the interface for allowing better collection of carriers. This would reduce the diffusion of carriers to the shunt path.

EQE

The EQE measurement is only possible on device SUB-5 because SUPER-18 showed too low of an efficiency to be properly measured. As mentioned in 3.4.3, losses occur throughout the device depending on multiple factors. These all contribute to the spectra of SUB-5 (see fig. 45).

By applying a reverse bias voltage of 0,5V, the space charge region increases. This is translates to an increase of the electron transport distance of the space charge region and thus increasing the carrier collection length and EQE. This is visible on the red and blue spectra. Efficiency increases about 10-15% when applying this bias voltage. Indicating that this device has diffusion length issues in the absorber. Possible factors that impact diffusion length are: presence of defects, etc.

When SUB-5 is exposed by bias light, the green and blue spectra are basically the same. There are no recombination centers visible. This might indicate that there is no interface recombination. If the device would be effected by interface recombination, the spectra when exposed to monochromatic light would differ from the spectra when exposed to bias light. This confirms the good compatibility of the used layers.

4.2 SEM imaging

SUB-5

Being one of the only devices showing an efficiency, SUB-5 is used as a reference device with the following configuration: Mo/Sb_2Se_3/CdS/ZnO/ITO. Cross sectional and top view images are taking by SEM. Figure 46 shows the layer structure, each layer is indicated and thicknesses are measured.

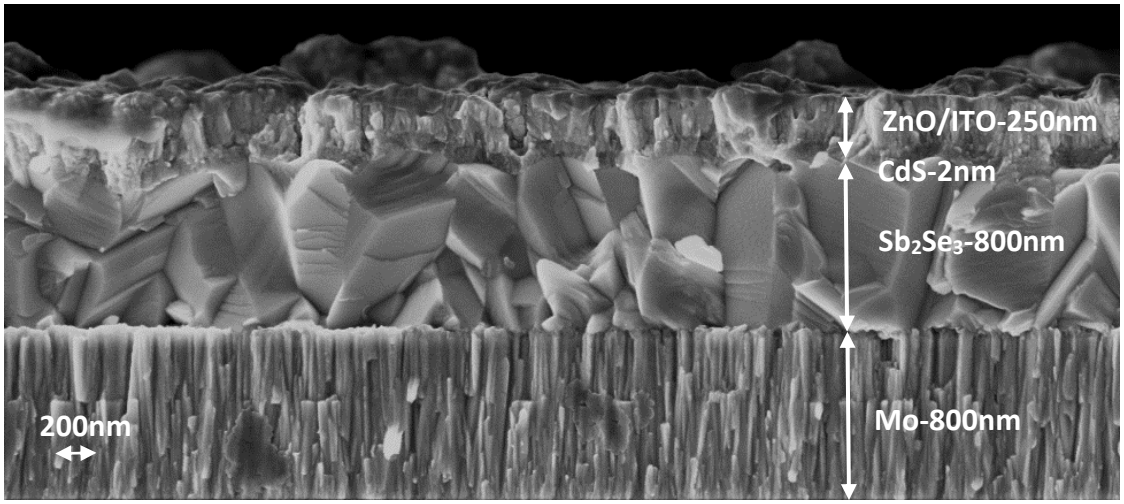

Figure 46: Cross sectional SEM image of SUB-5.

Figure 47 shows a top view image of device SUB-5. This image gives an idea of surface morphology of Sb_2Se_3 with the visible grains and the ZnO/ITO layer on top.

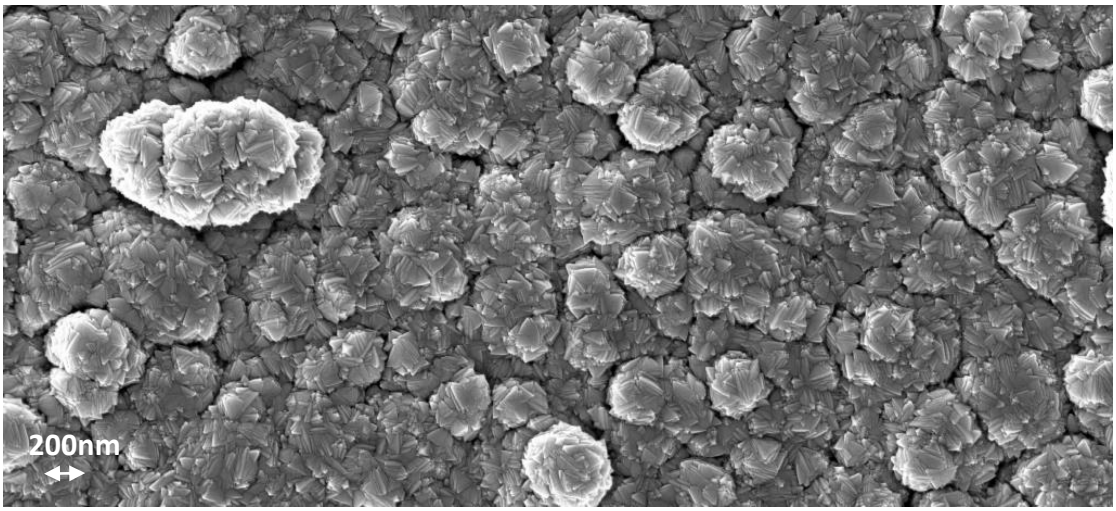

Figure 47: Top view SEM image of SUB-5.

Figure 48 shows a second top view of the SUB-5 surface. This image is taken in the Ag grid region of the device. It appears that a substantial part of top layer(s) is removed near the contact point of the measurement probes. It is not clear which layer is specifically visible in this region marked by '???'.

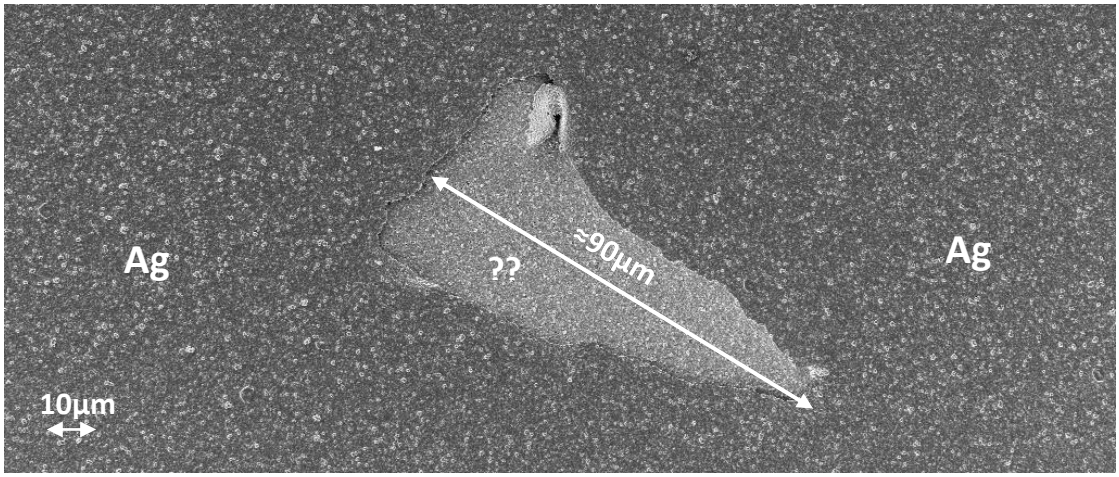

Figure 48: Top view SEM image of SUB-5 in the Ag grid region.

SUB-1

Device SUB-1 has the closest similarity in configuration as SUB-5, the difference being the Sb_2Se_3 and SbSeI absorber respectively. The complete SUB-1 configuration is the following: Mo/Sb_2Se_3/CdS/ZnO/ITO. SEM images are taken from the cross section and top view. Figure 49 shows a cross sectional SEM image. The distinctive metal chalcohalide columnar structures are clearly visible and seem to be (partially to fully) coated with different materials. An assumption of visible layers and thicknesses or structure lengths is done. It is especially hard to identify specific layers because these structures do not represent a thin film.

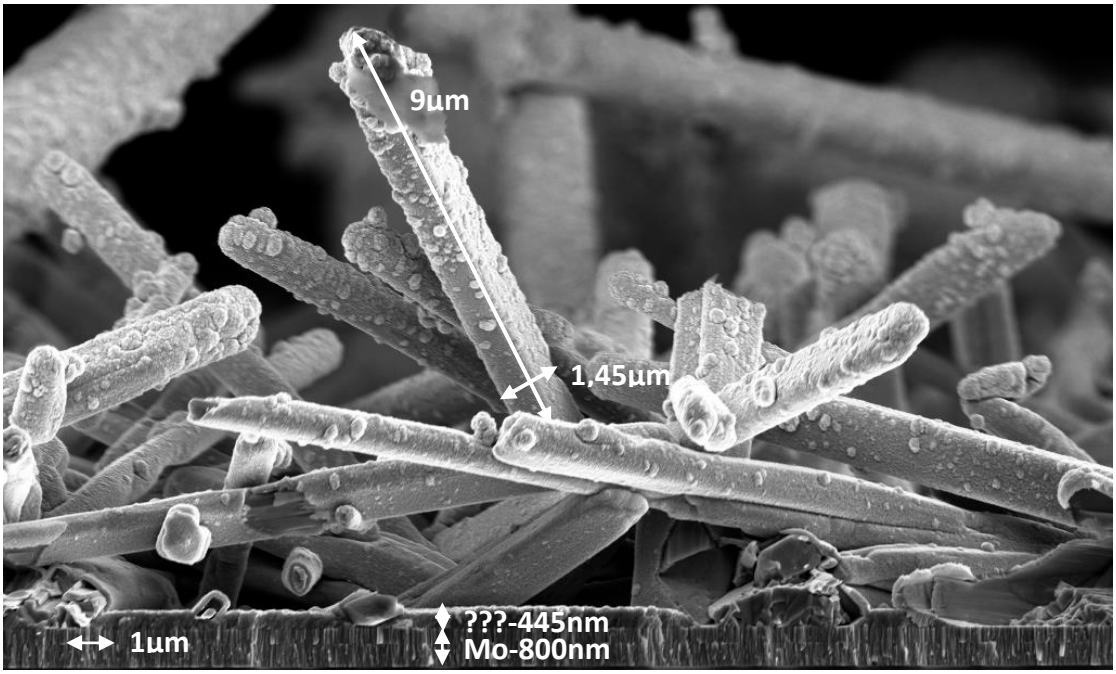

Figure 49: Cross sectional SEM image from SUB-1.

Figure 50 shows an uneven morphology of SUB-1. The underlying layers are visible, which layer is exactly seen on the image is unclear and is indicated as '???'.

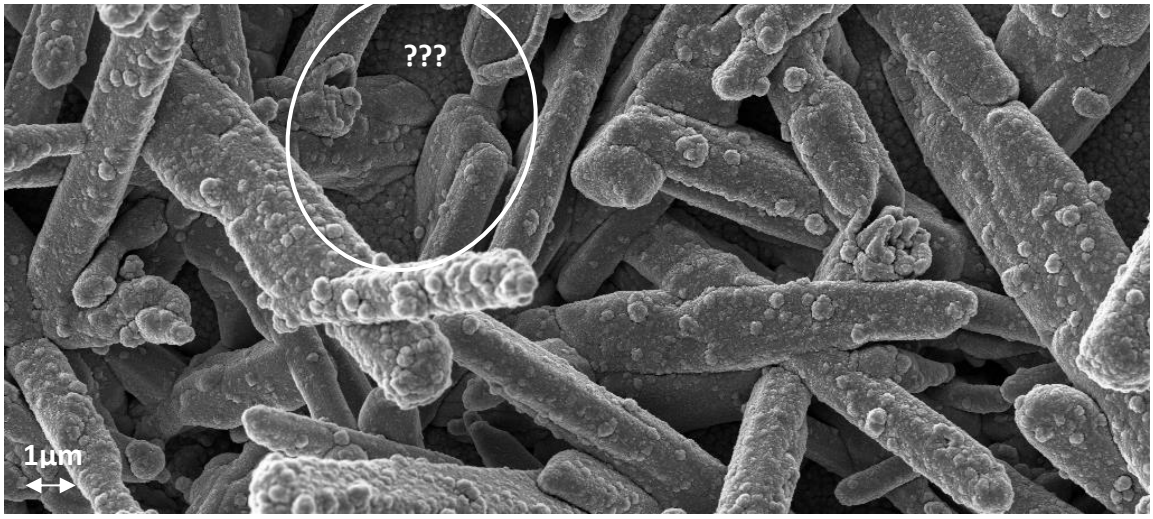

Figure 50: Top view SEM image of SUB-1.

SUB-6

Device SUB-6 did not show any efficiencies and consists of the following configuration: Mo/Sb_2Se_3/TiO_2/ZnO/ITO. This device is intended to be used as a reference for SUB-3. Figure 51 shows the thin film with the different layer materials and thicknesses.

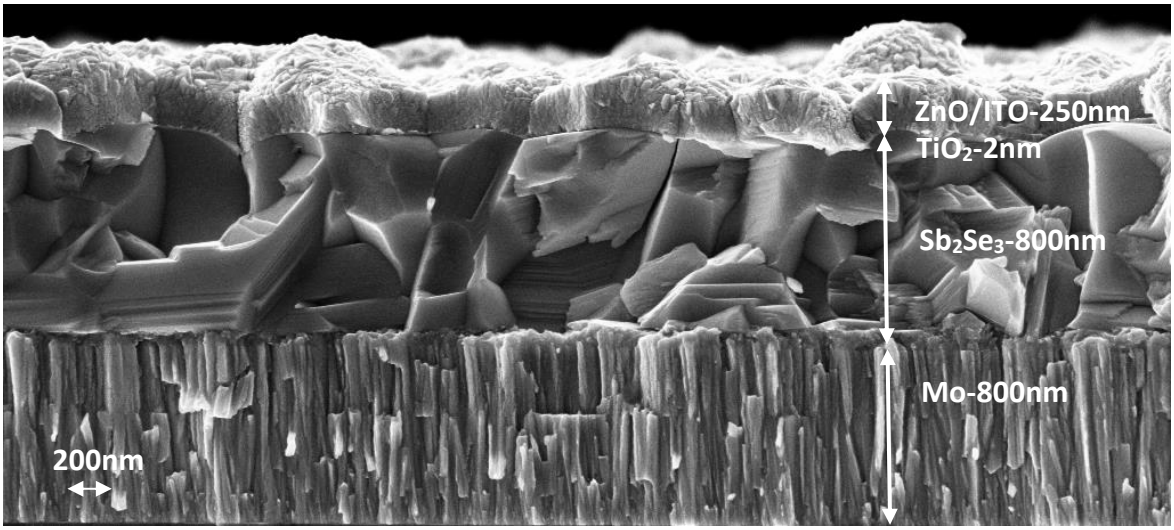

Figure 51: Cross sectional SEM image of SUB-6.

SUB-3

As mentioned above, device SUB-3 has the same layer configuration as SUB-6 apart from the absorbers being SbSeI and Sb_2Se_3 respectively. This device did not show any efficiencies and has the following configuration: Mo/SbSeI/TiO_2/ZnO/ITO. Figure 52 shows a cross sectional image. The same observations are made as for device SUB-1. An important observation is made of a region of unreacted Sb_2Se_3 precursor.

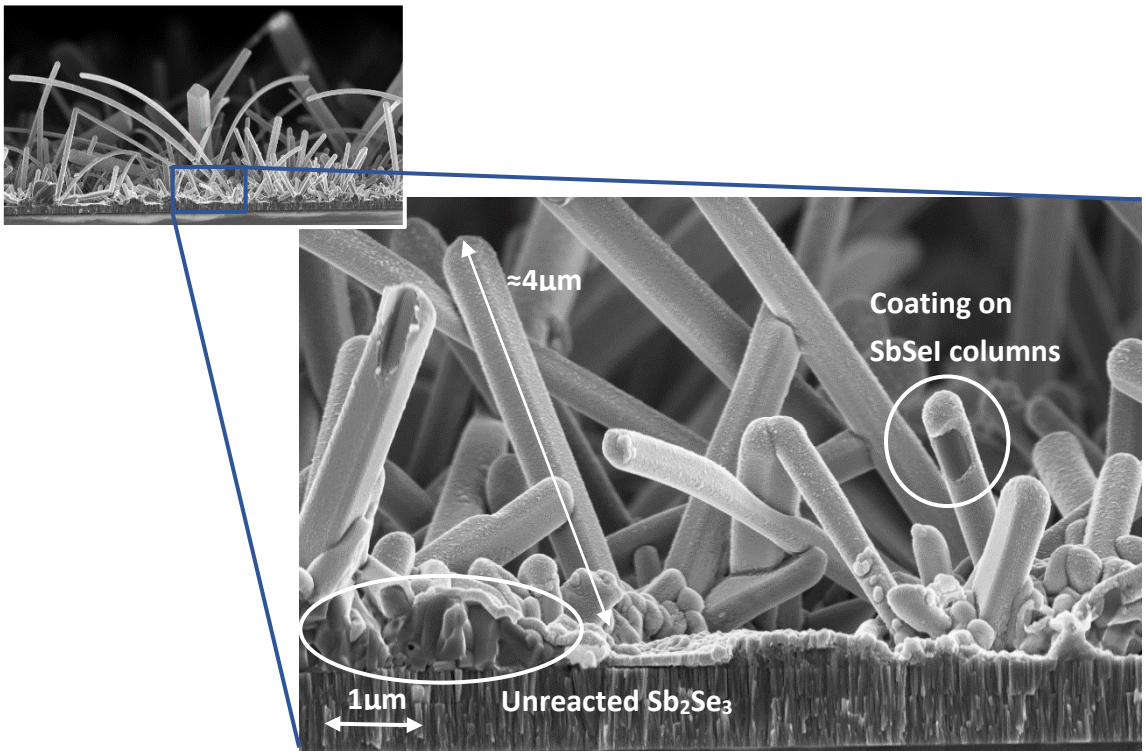

Figure 52: Cross sectional SEM image of SUB-3.

Figure 53 shows a top view SEM image of the silver grid of SUB-3. A large area of destroyed structures is visible. In between the damaged structures the underlying layers even become visible, as highlighted by the circles. Assumably these are the contact points of the measurement probes. The visible underlying layers seem to be either unreacted Sb_2Se_3 or Mo.

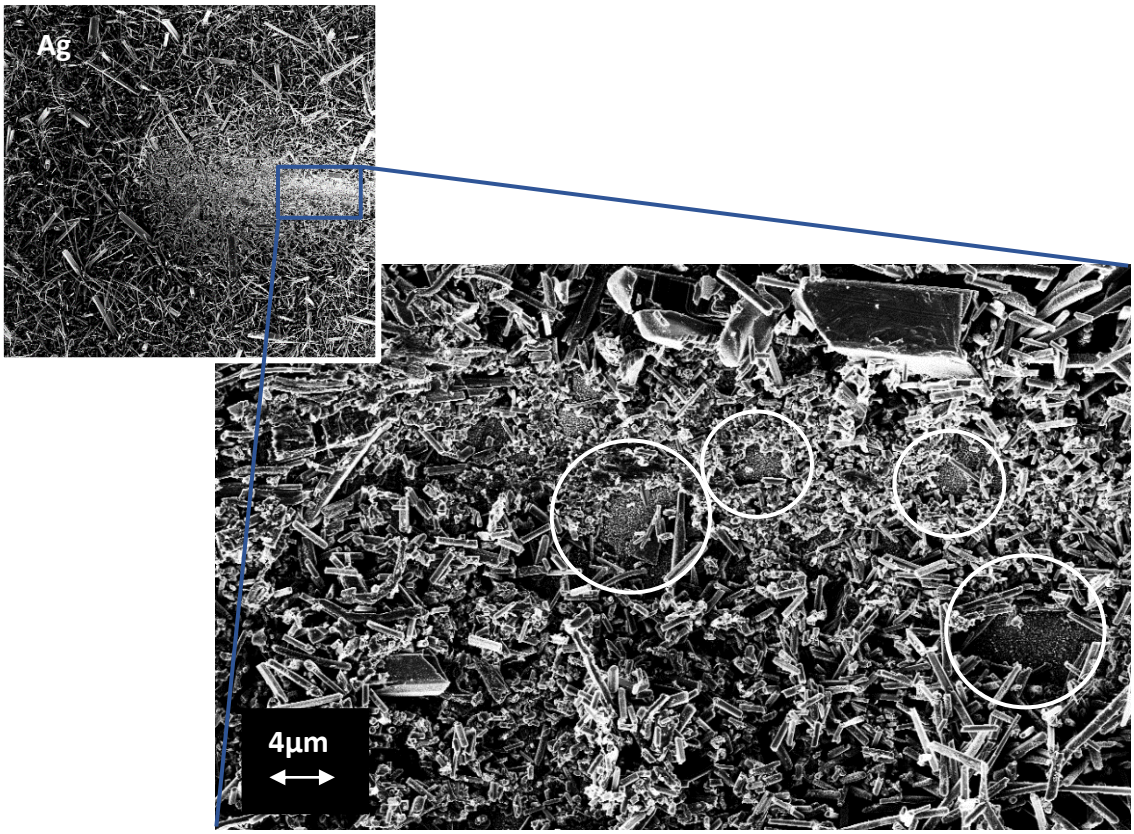

Figure 53: Top view SEM images of SUB-3.

SUPER-18

SUPER-18 is the second device that showed an efficiency, all be it very low. This is a superstrate configuration device, containing the following layers: FTO/CdS/Sb_2Se_3/MoO_3. Figure 54 shows a cross sectional image with the respective thin film layers and corresponding thicknesses.

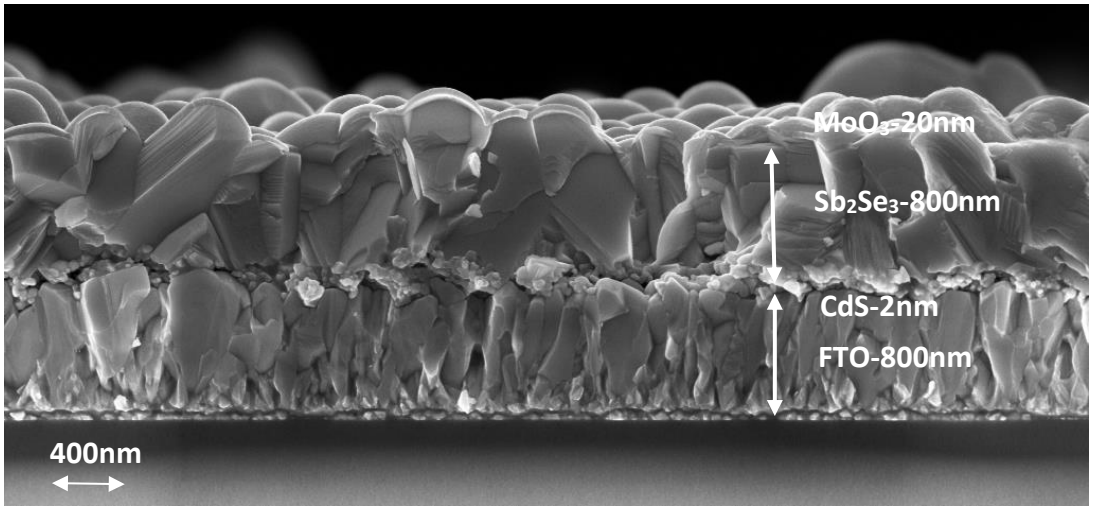

Figure 54: Cross sectional SEM image of SUPER-18.

The following image is from the same device, but highlights the gold contact layer. An important observation in this image is the difficult identification of the MoO3 layer. This layer should be present underneath the Au layer.

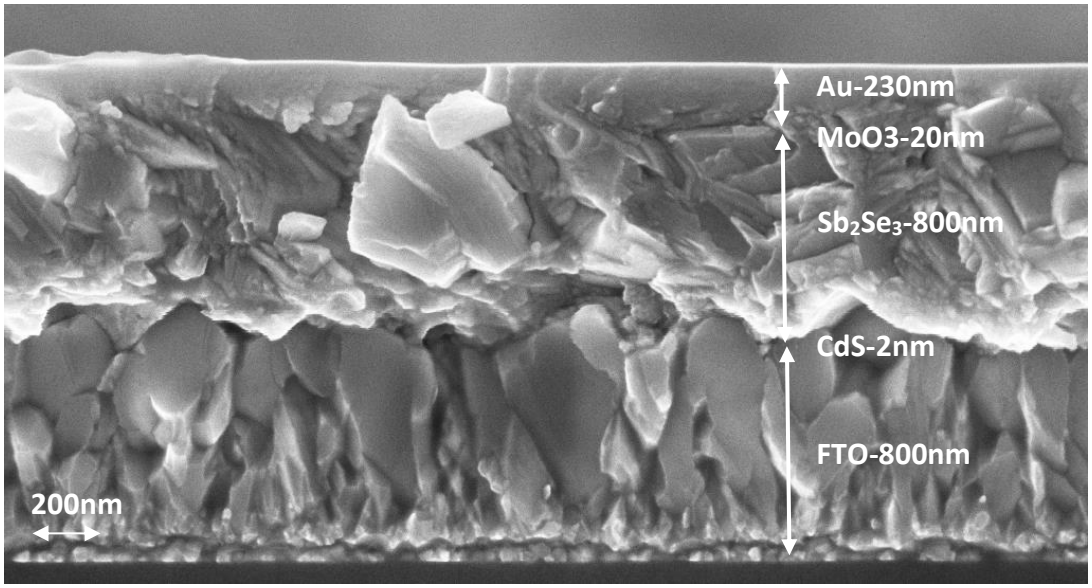

Figure 55: Cross sectional SEM image of SUPER-18 in the Ag contact region.

SUPER-16

SUPER-16 uses the similar layer configuration as SUPER-18, apart from the absorber. The exact configuration is the following: FTO/CdS/SbSeI/MoO_3. Figure 56 shows a cross sectional image of SUPER-16. The same observations are made with previous superstrate devices using SbSeI as absorber. Some of the columnar structures are 10's of micrometers in height. In the image all precursor seems to have reacted to SbSeI, but there are still some strange formations near the superstrate. The snow-like layer on top of the ribbons seems to be the gold layer, deposited by evaporation.

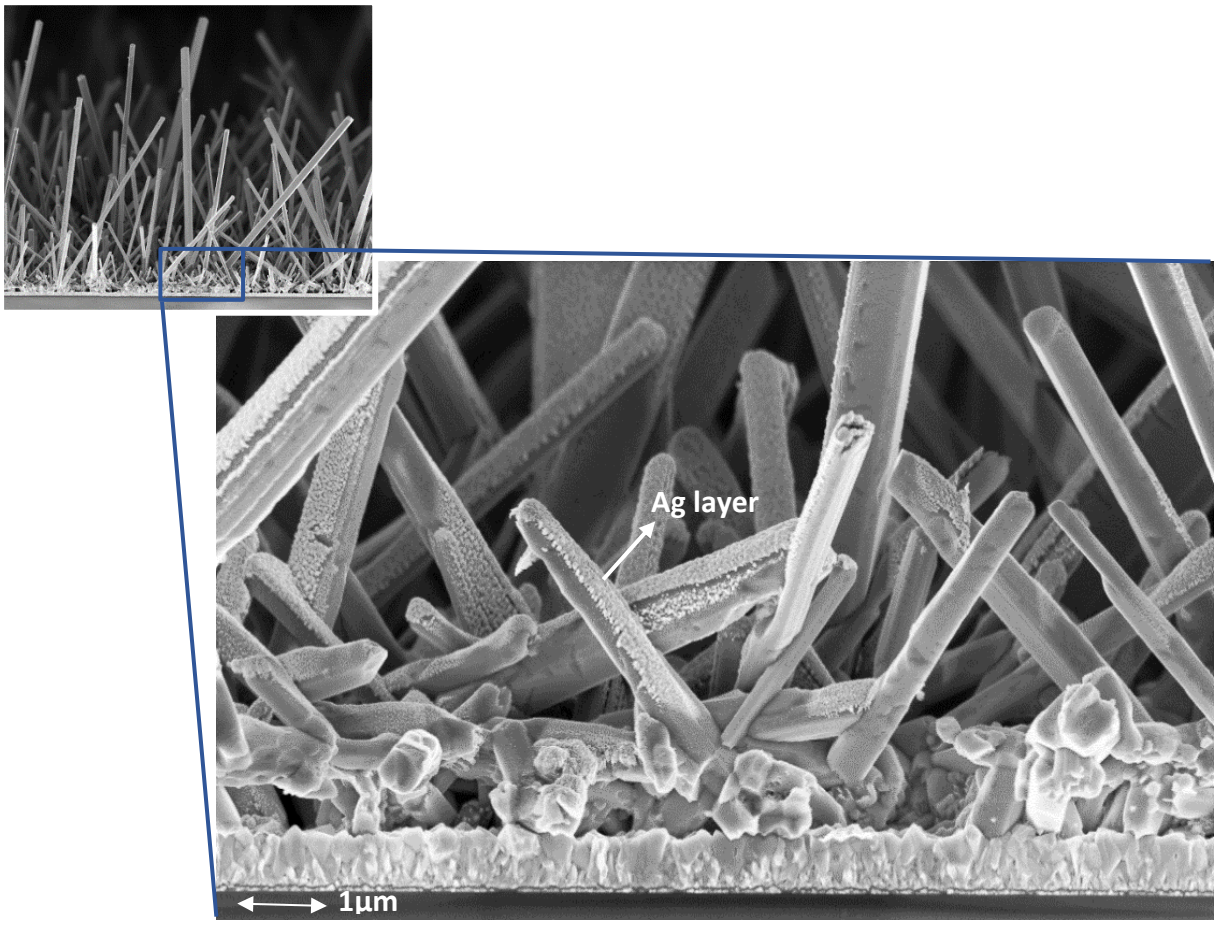

Figure 56: Cross sectional SEM image of SUPER-16.

SUPER-8

SUPER-8 has the following layer configuration: FTO/V_2O_5/SbSeI/MoO_3/PEDOT. This device did not show any efficiency, but still shows some interesting features. Figure 57 shows a cross sectional image of this device. The presence of columnar structures is seen on the image, but they appear to be broken off or damaged. Spin coating is used to deposit PEDOT (pH 1000), which is deposited after the formation of the ribbons. Due to the curvature of the structures, there seems to be a layer of PEDOT present on top.

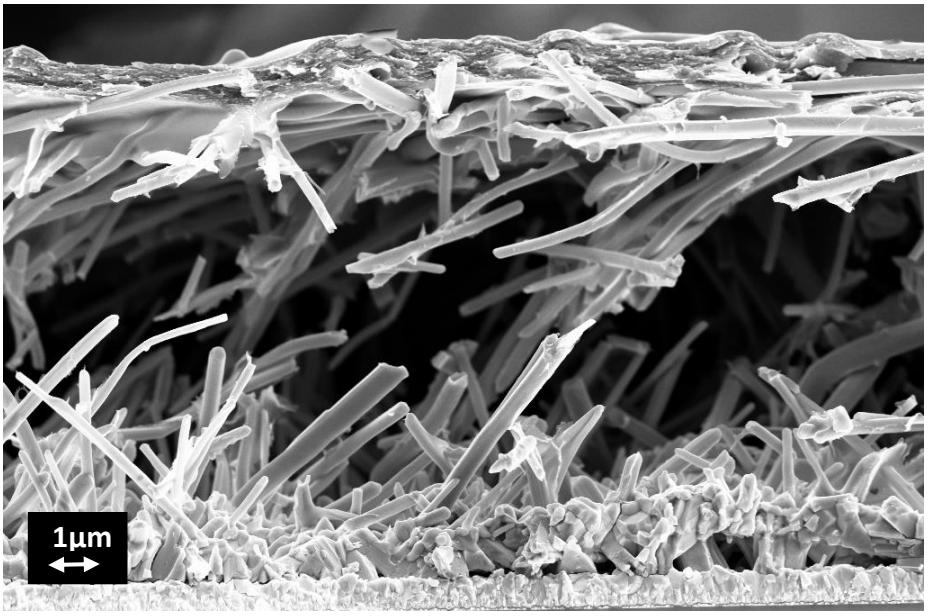

Figure 57: Cross sectional SEM image of SUPER-8.

4.2.1 Discussion

Firstly, it seems that the assumption made in the discussion 4.1.5 might hold a certain truth. The same coverage problems happen in the SbSeI devices produced for this thesis. These could lead to shunt paths that decrease the shunt resistance and thereby decrease J_{sc}. Resulting in a lowered efficiency. If this happens on a large scale, it is impossible to collect any carriers at the contacts.

A possible solution for this could be a passivation layer that creates increases the shunt resistance. This basically means it would be harder for carriers to travel down the ETL to a potential shunt path. Instead, this would encourage carriers to drift to the contacts.

A second observation is the sensitive nature of these relatively large columnar structures. Upon touching the uneven morphology by hand or by a probe, the structures seem to be easily destroyed. This could result in front contact probes hitting the back contact directly, negatively impacting measurements. Similarly for some deposition techniques, like spin coating, forces like centrifugal forces might damage or even break these structures.

Lastly, Au deposition seems to destroy the MoO_3 layer. Both layers are deposited via thermal evaporation, the higher power (= higher temperature) needed to evaporate Au seems to impact the MoO_3 layer.

4.3 XRD measurements

The goal of this measurement is to analyze the absorber crystalline structure. Figure 58 shows a diffractogram of 4 selected devices indicated by a different color. These patterns are compared with the diffractogram of pure absorbers Sb_2Se_3 and SbSeI in powder form, seen in black and grey. Devices SUB-2 and SUPER-12 contain a SbSeI absorber while SUB-6 and SUPER-28 contain Sb_2Se_3.

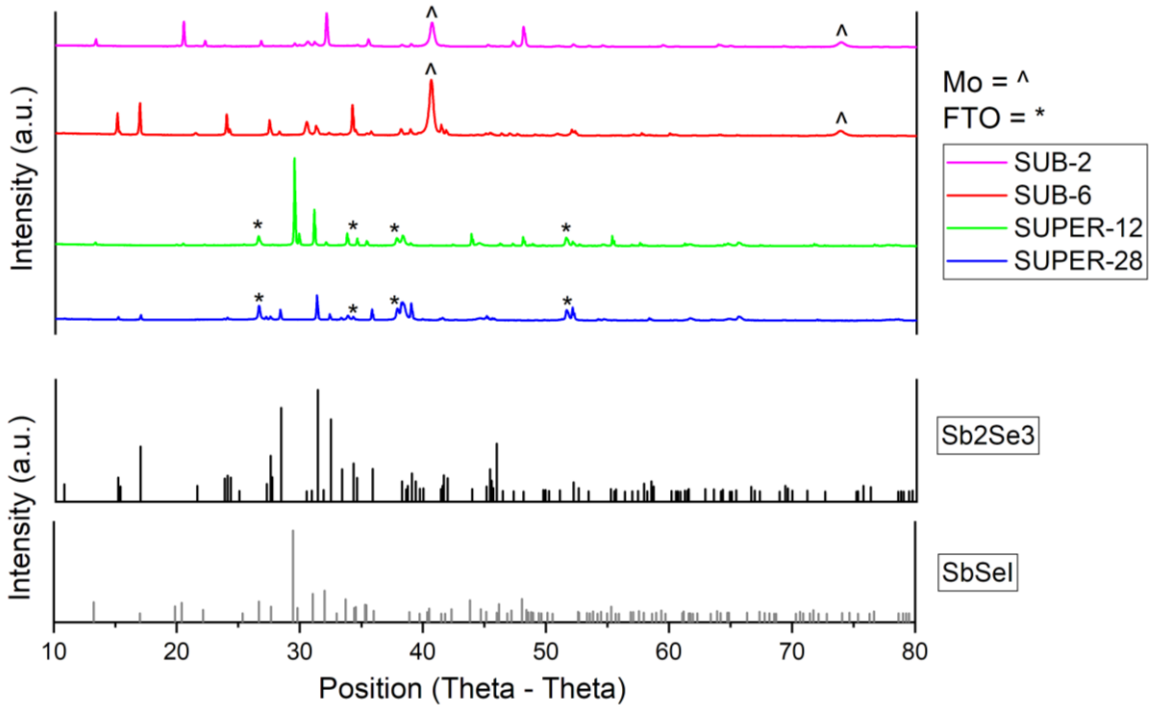

Figure 58: Diffractogram of SUB-2, SUB-6, SUPER-12 and SUPER-28.

4.3.1 Discussion

Comparing device diffractograms to the experimental powder pattern, shows some non-matching intensities indicated by symbols '*' and '^". These are visible phases of FTO and Mo which are expected in the superstrate and substrate devices respectively.

Comparing the rest of the patterns to their respective experimental diffractogram shows no other non-matching intensities. This indicates that the reaction has been completed with little to no other phases. This indicates that the synthesis process results in pure material.

According to [33], the experimental fingerprint patterns show the absorber material in powder form. A powder shows random crystalline orientations, the SbSeI based device diffractograms show similar intensities. This indicates a similar crystalline orientation as the experimental material or in other words a random crystalline orientation. The opposite happens for Sb_2Se_3 based devices with a clear matching of angle θ positions , but not in terms of intensity, this indicates a particular crystalline orientation.

5 Conclusion

It seems that band alignment is not the main problem of synthesizing devices with Sb_2Se_3 and SbSeI absorbers. Most likely, the formed columnar structures in the absorber layers, seem to be the main cause for non-working devices. The structures are relatively large, up to 10's of micrometers and randomly orientating, resulting in a very uneven morphology. Effectively, the structures do not form a thin film anymore. A trend is found under same pressure conditions (2bar). Increasing the process temperature, more Sb_2Se_3 precursor reacts with the SbI_3 source decreasing the coverage of the columns on the layers underneath. Depositing any type of contact layer on these columns increases the amount of shunt paths, negatively impacting efficiency.

Only two of the reference devices using Sb_2Se_3 seem to have worked, which was not expected. EQE measurements of one of the two working devices showed good compatibility of the layers. But due to the difference of spectra when applying a bias voltage indicate diffusion length issues in the absorber. A possible causes could be the presence of defects.

On the SEM images, large damaged area's with broken structures are observed. Presumably the contact point of measurement probes. This could negatively impact device measurements.

The diffractograms between devices containing Sb_2Se_3 and SbSeI show a clear difference. Devices that are synthesized using the Sb_2Se_3 absorber show a more similarly orientated crystallinity compared to devices using the SbSeI absorber. The latter seems to have a random crystalline orientation, which is unfavorable in solar cells.

5.1 Future work

Future work will have to focus on minimizing column height and orientation, and trying to optimize layer coverage in order to reduce possible shunt paths. A type of passivation layer could help improve efficiencies. Reducing the height and increasing the density of the columns could increase their strength to withstand external forces.

References

[1] “Strategic Energy Technology Plan,” Energy, 2018. https://energy.ec.europa.eu/topics/research-and-technology/strategic-energy-technology-plan_en (accessed Sep. 27, 2022).

[2] “Sensate | Partners,” Sensate.eu, 2020. http://sensate.eu/partners/ (accessed Oct. 11, 2022).

[3] “Novel low-dimensional chalcohalide materials for advanced integration of photovoltaic devices (MATER-ONE) PDF,” Memoria científico-técnica de proyetos coordinados, 2020.

[4] O. Isabella, Klaus Jäger, A. Smets, M. Zeman, and René van Swaaij, Solar Energy. 2016. Accessed: Oct. 14, 2022. [Online]. Available: https://research.tudelft.nl/en/publications/solar-energy-the-physics-and-engineering-of-photovoltaic-conversi

[5] S. M. Sze, Y. Li, and K. K. Ng, Physics of Semiconductor Devices. John Wiley & Sons, 2021. Accessed: Oct. 26, 2022. [Online]. Available: https://www.wiley.com/en-us/Physics+of+Semiconductor+Devices,+4th+Edition-p-9781119429111

[6] “The P-N Junction,” Gsu.edu, 2022. http://hyperphysics.phy-astr.gsu.edu/hbase/Solids/pnjun.html#c1 (accessed Nov. 03, 2022).

[7] “Band Theory for Solids,” Gsu.edu, 2022. http://hyperphysics.phy-astr.gsu.edu/hbase/Solids/band.html#c1 (accessed Oct. 26, 2022).

[8] Y. Li, “Synthesis, Characterization, and Photovoltaic Applications of Mesoscopic Phthalocyanine Structures,” ResearchGate, Nov. 10, 2011. https://www.researchgate.net/publication/301613152_Synthesis_Characterization_and_Photovoltaic_Applications_of_Mesoscopic_Phthalocyanine_Structures (accessed Nov. 06, 2022).

[9] “Natural Band Alignments and Band Offsets of Sb2Se3 Solar Cells,” ACS Applied Energy Materials, 2020. https://pubs.acs.org/doi/10.1021/acsaem.0c01477 (accessed Nov. 09, 2022).

[10] Wikipedia Contributors, “Thin-film solar cell,” Wikipedia, Oct. 27, 2022. https://en.wikipedia.org/wiki/Thin-film_solar_cell (accessed Nov. 09, 2022).

[11] Z. Liu, “Optical loss analysis of silicon wafer based solar cells and modules,” ResearchGate, Dec. 31, 2016. https://www.researchgate.net/publication/319141094_Optical_loss_analysis_of_silicon_wafer_based_solar_cells_and_modules (accessed Nov. 09, 2022).

[12] Z. Duan et al., “Sb_2Se_3 Thin-Film Solar Cells Exceeding 10% Power Conversion Efficiency Enabled by Injection Vapor Deposition Technology,” Advanced Materials, vol. 34, no. 30, p. 2202969, Jun. 2022, doi: 10.1002/adma.202202969.

[13] Y. Zhou et al., “Thin-film Sb2Se3 photovoltaics with oriented one-dimensional ribbons and benign grain boundaries,” Nature Photonics, vol. 9, no. 6, pp. 409–415, May 2015, doi: 10.1038/nphoton.2015.78.

[14] K. Zeng, D.-J. Xue, and J. Tang, “Antimony selenide thin-film solar cells,” Semiconductor Science and Technology, vol. 31, no. 6, p. 063001, Apr. 2016, doi: 10.1088/0268-1242/31/6/063001.

[15] F. Palazon, “Metal Chalcohalides: Next Generation Photovoltaic Materials?,” Solar RRL, vol. 6, no. 2, p. 2100829, Dec. 2021, doi: 10.1002/solr.202100829.

[16] Wikipedia Contributors, “Evaporation (deposition),” Wikipedia, Oct. 05, 2021. https://en.wikipedia.org/wiki/Evaporation_(deposition) (accessed Nov. 29, 2022).

[17] C. Adachi, R. Hattori, H. Kaji, and T. Tsujimura, “Handbook of Organic Light-Emitting Diodes,” SpringerLink, 2020, doi: 10.1007-978-4-431-55761-6.

[18] Wikipedia Contributors, "Atomic layer deposition," Wikipedia, Sep. 22, 2022. https://en.wikipedia.org/wiki/Atomic_layer_deposition (accessed Dec. 16, 2022).

[19] Wikipedia Contributors, "Thin-film thickness monitor," Wikipedia, May 22, 2022. https://en.wikipedia.org/wiki/Thin-film_thickness_monitor (accessed Dec. 12, 2022).

[20] Wikipedia Contributors, "Quartz crystal microbalance," Wikipedia, Oct. 25, 2022. https://en.wikipedia.org/wiki/Quartz_crystal_microbalance (accessed Dec. 12, 2022).

[21] Wikipedia Contributors, "Sputter deposition," Wikipedia, Aug. 22, 2022. https://en.wikipedia.org/wiki/Sputter_deposition#High-power_impulse_magnetron_sputtering_(HiPIMS) (accessed Nov. 30, 2022).

[22] "(1) (PDF) Preparation of Pure Anatase TiO2 Thin Films by DC Sputtering Technique: Study on the Effect of Oxygen Partial Pressure," ResearchGate, 2012, doi: 10.4028\/www.scientific.net\/AMR.463-464.1415.

[23] N. Maticiuc, J. Hiie, and T. Potlog, "Mechanism of Changes in the Properties of Chemically Deposited CdS Thin Films Induced by Thermal Annealing," Taltech.ee, Nov. 25, 2015. https://digikogu.taltech.ee/et/Item/26f17525-502e-43a1-a94e-03b043736e90 (accessed Dec. 02, 2022).

[24] Wikipedia Contributors, "Chemical bath deposition," Wikipedia, Aug. 04, 2022. https://en.wikipedia.org/wiki/Chemical_bath_deposition#Photovoltaics (accessed Dec. 02, 2022).

[25] "Crystal Growth Promotion and Defect Passivation by Hydrothermal and Selenized Deposition for Substrate-Structured Antimony Selenosulfide Solar Cells," ACS Applied Materials & Interfaces, 2022. https://pubs.acs.org/doi/10.1021/acsami.2c06805 (accessed Dec. 01, 2022).

[26] "MTI Corp - Leading provider of lab equipments and advanced crystal substrates," MTI Corp - Leading provider of lab equipments and advanced crystal substrates, 2022. https://www.mtixtl.com/highpressurefurnacehip.aspx (accessed Dec. 21, 2022).

[27] Wikipedia Contributors, "Spin coating," Wikipedia, Nov. 28, 2022. https://en.wikipedia.org/wiki/Spin_coating (accessed Dec. 17, 2022).

[28] Wikipedia Contributors, "PEDOT:PSS," Wikipedia, Feb. 22, 2022. https://en.wikipedia.org/wiki/PEDOT:PSS (accessed Dec. 19, 2022).

[29] D. Abou-Ras, T. Kirchartz, and U. Rau, Eds., Advanced Characterization Techniques for Thin Film Solar Cells. Wiley, 2011. doi: 10.1002/9783527636280.

[30] P. Paulissen, "Feasibility of artificial synapses using thin film photovoltaic materials and architectures," Uhasselt.be, 2022, doi: http://hdl.handle.net/1942/38255.

[31] AZoM, "Unmasking Microabsorption: Why Fluorescence Suppression in Powder XRD Does More Harm Than Good," AZoM.com, Jan. 05, 2021. https://www.azom.com/article.aspx?ArticleID=20003 (accessed Jan. 10, 2023).

[32] "X-Ray Diffraction (XRD) | Braggs Equation & Applications of XRD," Lets Talk Academy, 2021. https://letstalkacademy.com/x-ray-diffraction/ (accessed Jan. 11, 2023).

[33] "Does Sb2Se3 Admit Nonstoichiometric Conditions? How Modifying the Overall Se Content Affects the Structural, Optical, and Optoelectronic Properties of Sb2Se3 Thin Films," ACS Applied Materials & Interfaces, 2022. https://pubs.acs.org/doi/full/10.1021/acsami.1c20764 (accessed Jan. 19, 2023).

Appendices

Appendix A: Work Plan ……60
Appendix B: Presentation SeeFuturePV ……62
Appendix C: Poster IEEE Ivan Caño ……70

Appendix A:

Fabrication of thin film solar cells: substrate configuration

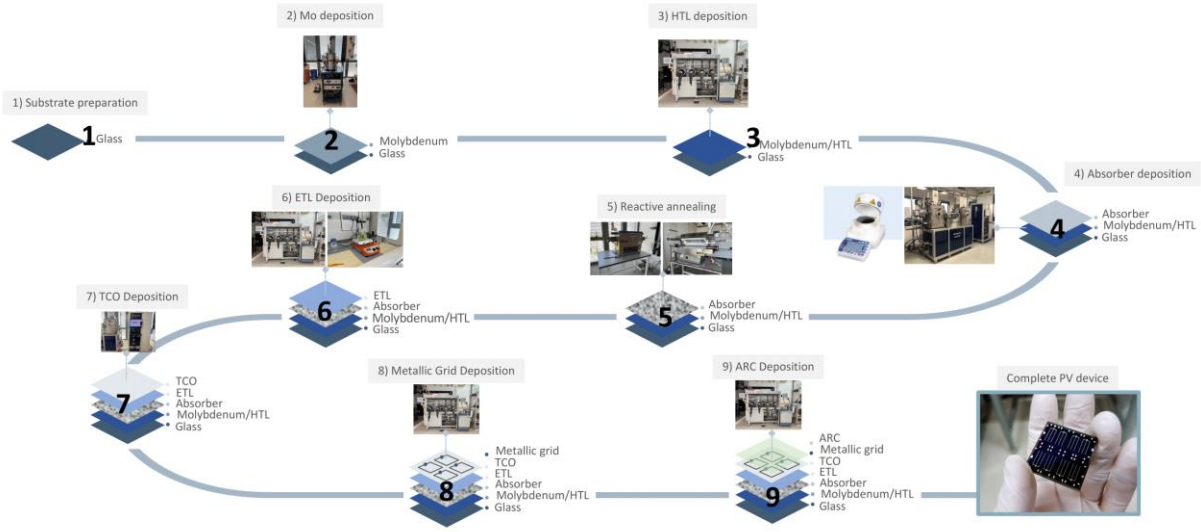

Objectives of Sander Moens Thesis

The general objective is to investigate the best suited device architecture and holes/electrons selective contacts for emerging thin film van der Waals photovoltaic technologies based on SbSeI and SbSeBr mixed chalco-halide compounds. This will include the following sub-objectives:

- Synthesis of optimized SbSeI and SbSeBr thin films by a sequential process based on the co-evaporation of Sb_2Se_3 layers followed by a reactive annealing under high pressure and using SbI_3 as precursor, using the already developed technology at UPC
- Implementation of substrate and superstrate solar cells architectures using standard $MoSe_2$/CdS and Au/CdS as holes and electrons transport layers respectively
- Extension to the study of other possible selective contacts including TiO_2, V_2O_5, MoO_3 and PEDOT
- Fabrication and optoelectronic characterization of solar cell devices

Substrate configuration: study of different ETL's

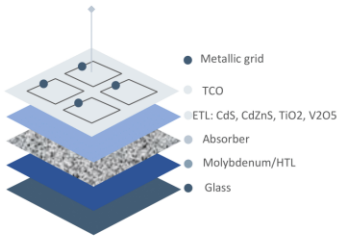

Superstrate configuration: study of different HTL's and ETL's

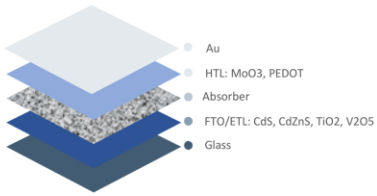

Appendix B:

UNIVERSITAT POLITÈCNICA DE CATALUNYA BARCELONATECH

IREC Shaping Energy for a Sustainable Future

See Future PV

Innovative quasi-1D SbSeI micro-columnar semiconductors for defect-tolerant, optically tuneable solar cells

Ivan Caño[1], Alejandro Navarro Güell[1], Sergio Giraldo[1], Maykel Jiménez Guerra[1], Alex Jiménez Arguijo[2], Joaquim Puigdollers[1], Marcel Placidi[1], Edgardo Saucedo[1]

SENSATE

[1] Photovoltaic Group, Polytechnic University of Catalonia (UPC), Barcelona (Barcelona)
[2] Catalonia Institute for Energy Research (IREC), Sant Adrià de Besòs (Barcelona)

1

CONTENTS

- Introduction
  - Quasi-1D chalcogenides
  - Why develop chalco-halide semiconductors?
- Experimental Procedure
- Results
- Conclusion and Next Steps

2

INTRODUCTION

Quasi-1D chalcogenides – New perspectives for the next generation PV

- Earth-abundant and low toxic constituents
- Stability. Synthesis at T < 400°C
- Excellent optoelectronic properties
- Quasi-1D structure

enhanced anisotropic electrical properties when material is correctly oriented[1]

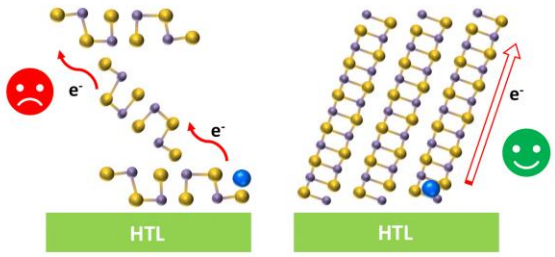

carriers "hopping" ribbon-assisted transport

recent successes of the quasi-1D chalcogenide system

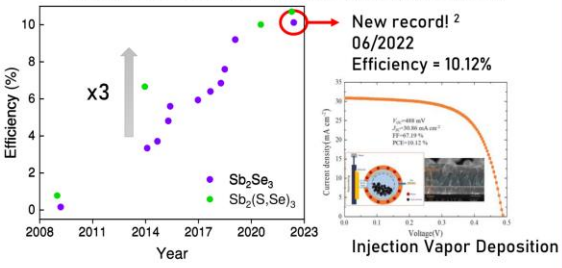

$Sb_2(S,Se)_3$ – 10.7% (2022) → Hydrothermal deposition[3]

[1] Y Xhow, L Wang, S Chen, S Qin, X Liu, J Chen, D Xue, M, Luo, Y Cao, Y Cheng, EH Sargent, J Tang, *Nature Photonics*, 2015, 5, 409
[2] Z Duan, X Liang, Y Feng, H Ma, B Liang, Y Wang, S Kuo, S Wang, REI Schropp, Y Mai, Z Li, *Advanced Materials*, 2022
[3] Y Zhao, S Wang, C Jiang, C Li, P Xiao, R Tang, J Gong, G Chen, T Chen, J Li, X Xiao, *Advanced Energy Materials*, 2022, 12, 2103015

INTRODUCTION

1D semiconductors beyond Sb_2Se_3 have been barely investigated for energy generation applications

5 B	6 C	7 N	8 O	9 F
13 Al	14 Si	15 P	16 S	17 Cl
31 Ga	32 Ge	33 As	34 Se	35 Br
49 In	50 Sn	51 Sb	52 Te	53 I
81 Tl	82 Pb	83 Bi	84 Po	85 At

covalent bonding → difference between the electronegativities of cations and anions needs to be lower than 1.7 eV

Sb_2Se_3 → ΔX = 0.5

SbSeI → ΔX = 0.6

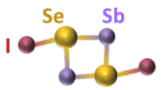

Why develop SbSeI?

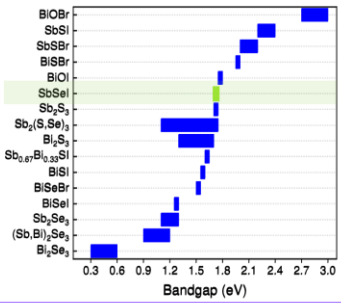

1. Relatively wide bandgap

SbSeI → Eg = 1.8 – 2.0 eV

- Tandem architectures
- Semi-transparent devices

2. Defect tolerant semiconductor[4]

a) Possesses few intrinsic / structural defects
b) Defects have a minimal effect on mobility and carrier lifetime

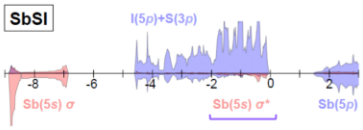

cation antibonding s-orbital contribution at the VBM

$MAPbI_3$ → defect tolerance emerges from having bonding orbitals at the CBM and antibonding orbitals at the VBM

[4] RE Brandt, V Stevanovic, DS Ginley, T Buonassisi, *MRS Communications*, 2015, 5, 265

INTRODUCTION

1D semiconductors beyond Sb_2Se_3 have been barely investigated for energy generation applications

5 B	6 C	7 N	8 O	9 F
13 Al	14 Si	15 P	16 S	17 Cl
31 Ga	32 Ge	33 As	34 Se	35 Br
49 In	50 Sn	51 Sb	52 Te	53 I
81 Tl	82 Pb	83 Bi	84 Po	85 At

covalent bonding → difference between the electronegativities of cations and anions needs to be lower than 1.7 eV

Sb_2Se_3 → ΔX = 0.5

SbSeI → ΔX = 0.6

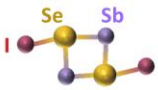

Why develop SbSeI?

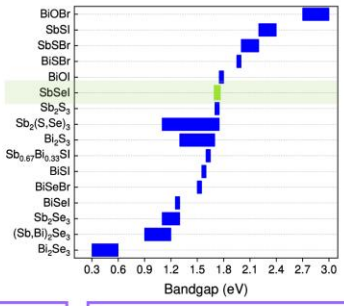

3. Ferroelectric properties

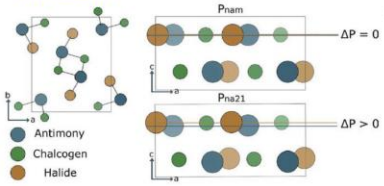

Ferroelectricity in SbSI

E. Fatuzzo, G. Harbeke, W. J. Merz, R. Nitsche, H. Roetschi, and W. Ruppel
Laboratories, RCA Ltd., Zurich, Switzerland
(Received May 11, 1962; revised manuscript received June 18, 1962)

Ferroelectric transition → ideal candidate for exhibiting both bulk and poly-crystalline photo-ferroic effects[5]

Photovoltage (V_{oc}) not limited by the bandgap

Ideal candidate for heterojunctions (SbSeI/SbSeBr)

4. Applications beyond photovoltaics

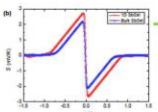

Seebeck coefficient Thermoelectrics[6]

Piezo- / triboelectric applications[7]

For the first time, the sample preparation method and application of SbSeI pellet as a nanogenerator combining principles of both triboelectric and piezoelectric effects have been presented. The

[5] KT Butler, JM Frost, A Walsh, *Energy & Environmental Science*, 2015, 8, 838
[6] B Peng, K Xu, H Zhang, Z Ning, H Shao, G Ni, J Li, Y Zhu, H Zhu, CM Soukalis, *Advanced Theory and Simulations*, 2018, 1, 1700005
[7] B Torún, K Mistewicz, M Jesionek, M Koziol, M Zubko, D Stróż, *Energy*, 2022, 238, 122048

5

EXPERIMENTAL PROCEDURE

Synthesis of SbSeI films: Mo/Sb_2Se_3 post-annealing under chalcogen (Se) and halogen (SbI_3) atmosphere

1. Substrate cleaning
2. Mo deposition → Glass/Mo
3. Sb deposition → Glass/Mo/Sb
4. Sb_2Se_3 synthesis → Glass/Mo/Sb_2Se_3
5. SbSeI synthesis → Glass/Mo/SbSeI

High pressure furnace: allows to control the I_2 partial pressure and avoid evaporation of volatile compounds at P atm, such as halides

6

RESULTS

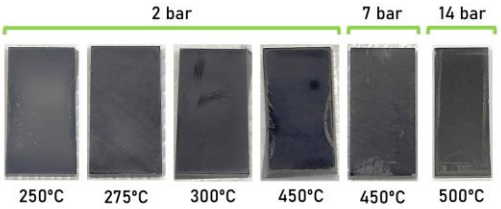

SEM – Formation of SbSeI micro-columnar structures

- Increasing T → height and density of micro-columnar structures increases
  Thickness and uniformity of unreacted Sb_2Se_3 layer decreases

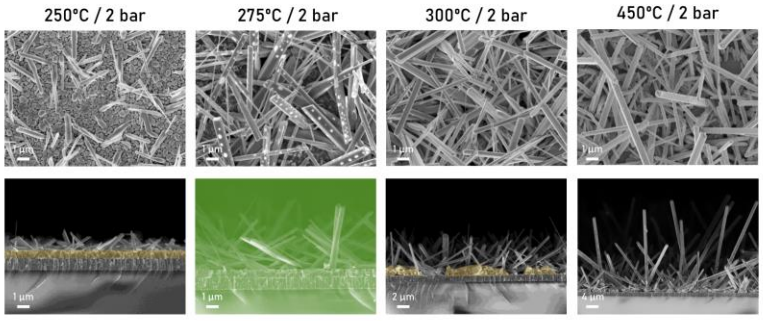

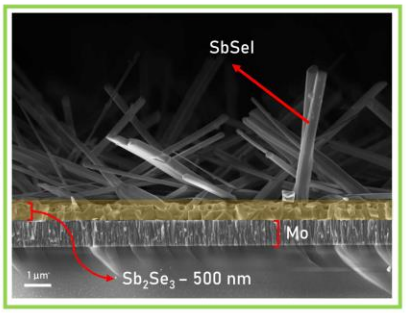

RESULTS

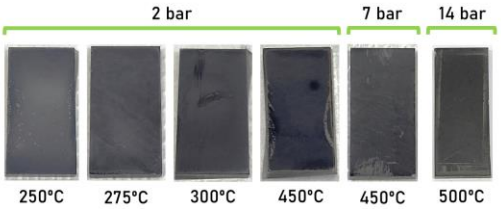

SEM – Formation of SbSeI micro-columnar structures

- Increasing T → height and density of micro-columnar structures increases
  Thickness and uniformity of unreacted Sb_2Se_3 layer decreases

Tunable morphology by modifying annealing conditions

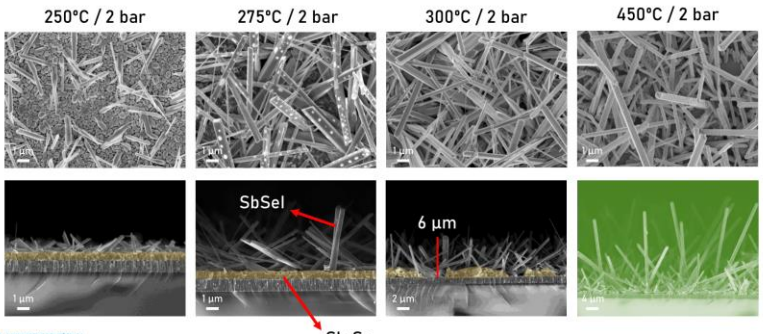

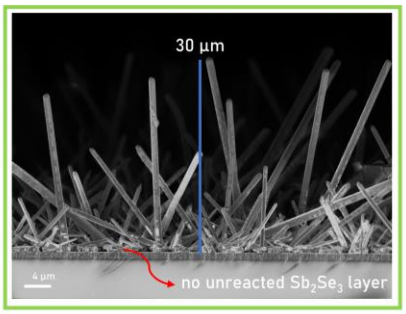

RESULTS

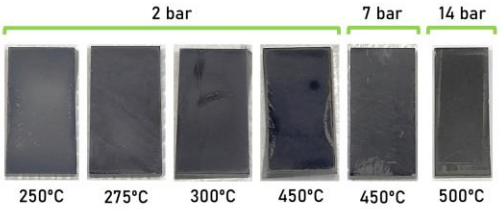

SEM – Formation of SbSeI micro-columnar structures

- Increasing T → height and density of micro-columnar structures increases
  Thickness and uniformity of unreacted Sb_2Se_3 layer decreases
- Increasing P → height of micro-columns decreases

Tunable morphology by modifying annealing conditions

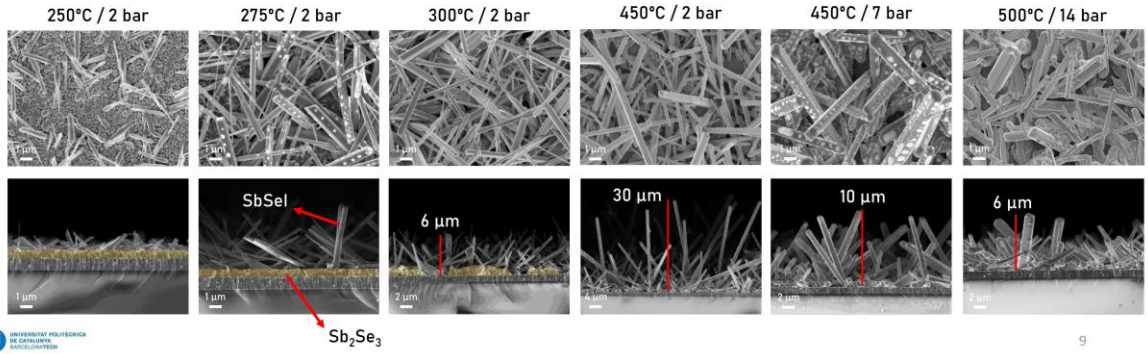

RESULTS

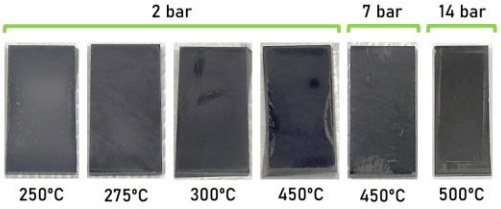

SEM – Formation of SbSeI micro-columnar structures

- Increasing T → height and density of micro-columnar structures increases
  Thickness and uniformity of unreacted Sb_2Se_3 layer decreases
- Increasing P → height of micro-columns decreases

Tunable morphology by modifying annealing conditions

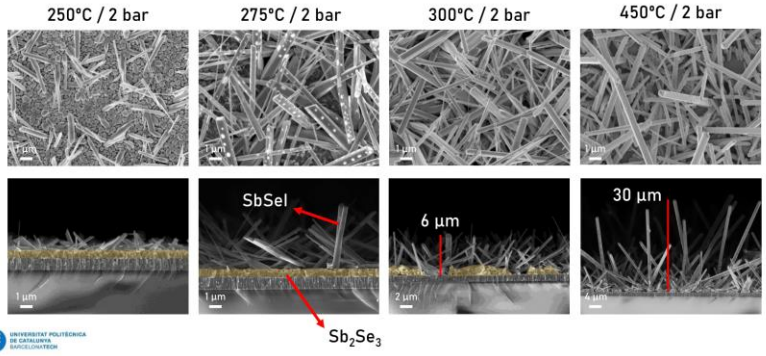

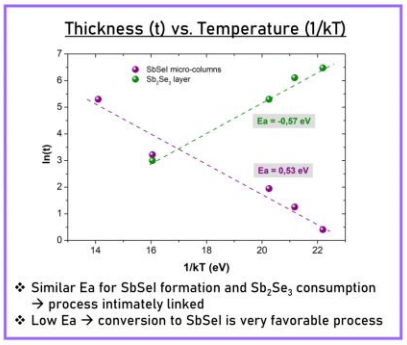

- Similar Ea for SbSeI formation and Sb_2Se_3 consumption → process intimately linked
- Low Ea → conversion to SbSeI is very favorable process

RESULTS

Structural and crystallographic characterization

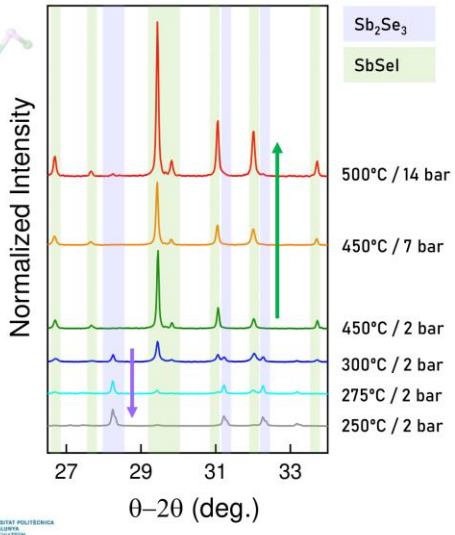

XRD – Detected phases of Sb_2Se_3 (unreacted layer) and SbSeI

- Sb_2Se_3 amount decreases as T increases
- Full conversion to SbSeI at 450°C – no preferred orientation

HR-TEM – Performed on a lamella of 450°C / 2 bar sample

- Excellent crystalline quality of micro-column structures
- Constituted by a single crystal – absence of grains

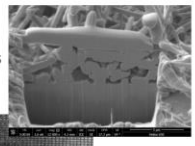

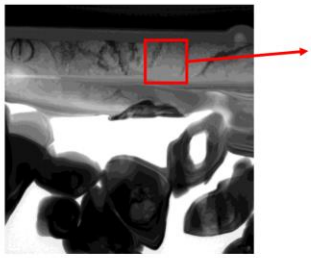

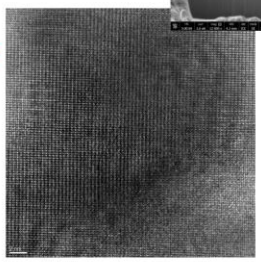

11

RESULTS: Formation mechanism model

1. Synthesis of Sb_2Se_3 thin films
2. Decomposition of SbI_3 to release I_2
3. Reaction of $I_{2(g)}$ with $Sb_2Se_{3(s)}$ to form $SbSeI_{(s)} + Se_{(l)}$
4. $SbSeI_{(s)}$ is dissolved into the liquid-Se phase
5. Precipitation of $SbSeI_{(s)}$ phase from the liquid-Se to form the micro-columnar structures

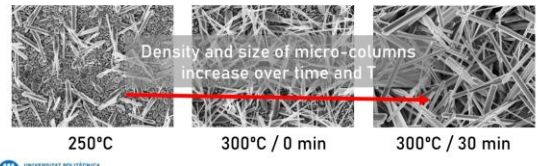

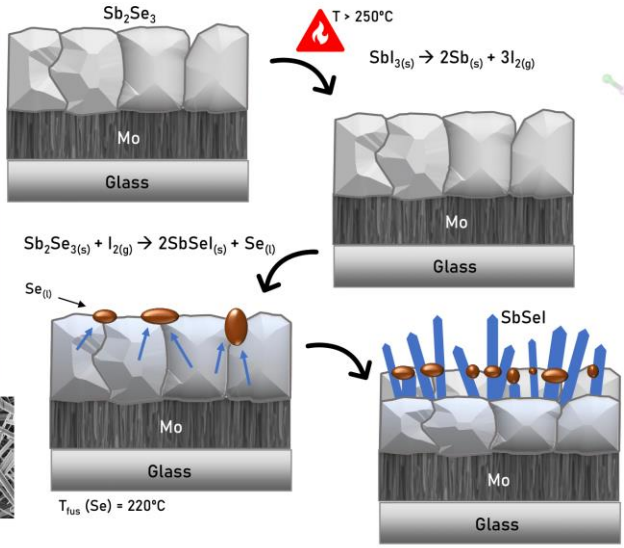

12

RESULTS

Optoelectronic characterization

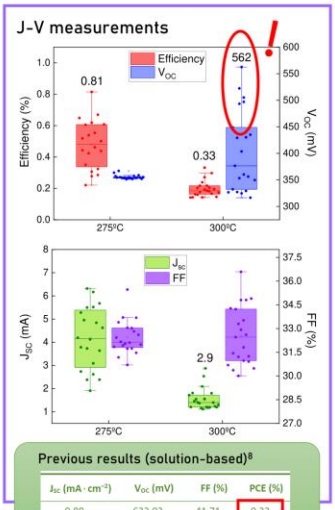

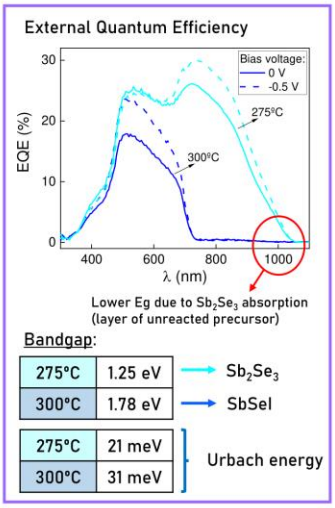

Bandgap:

275°C	1.25 eV	→ Sb_2Se_3
300°C	1.78 eV	→ SbSeI
275°C	21 meV	Urbach energy
300°C	31 meV	

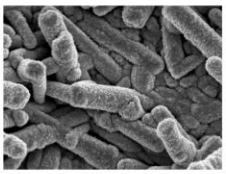

Mo/SbSeI/CdS/ZnO/ITO samples

300°C

- V_{oc} up to 550 mV (among the highest reported for SbSeI)
- Low Jsc & FF → poor carrier collection (columnar morphology)
- Bandgap of 1.8 eV – SbSeI is the dominant phase

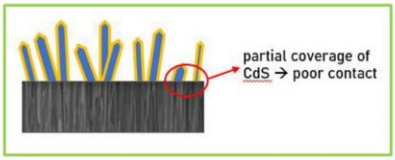

[8] YC Choi, K Jung, *Nanomaterials*, 2021, 11, 3206

CONCLUSIONS AND NEXT STEPS

- SbSeI micro-columnar samples have been synthesized by high-pressure iodination of Sb_2Se_3 thin films
  - Morphology can be tuned by varying annealing conditions (T and P)
  - Samples annealed at T ≤ 300°C → Sb_2Se_3 unreacted layer. Its amount decreases with increasing T
  - T = 450°C → Full conversion to SbSeI (no secondary phases)

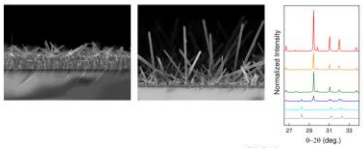

- Proposed formation model: columnar structures are form by a self-catalyzed SLV mechanism (solid-liquid vapor)
  - Decomposition of SbI_3 to realease $I_{2(g)}$
  - $Sb_2Se_{3(s)} + I_{2(g)} \rightarrow 2SbSeI_{(s)} + Se_{(l)}$
  - Precipitation of $SbSeI_{(s)}$ from the liquid-Se leads to formation of micro-columnar morphology

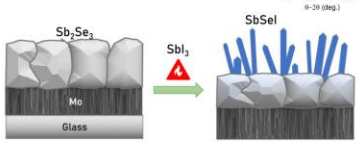

NEXT STEPS

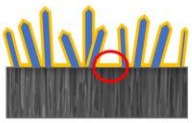

Improve front contact
↓
Full coverage by Atomic Layer Deposition (ALD)

Improve carrier collection → J_{sc} ↑

New selective contacts: oxides (TiO_2, VO_5)

Expand the family of quasi-1D chalco-halides

5 B	6 C	7 N	8 O	9 F
13 Al	14 Si	15 P	16 S	17 Cl
31 Ga	32 Ge	33 As	34 Se	35 Br
49 In	50 Sn	51 Sb	52 Te	53 I
81 Tl	82 Pb	83 Bi	84 Po	85 At

SbSeBr
BiSeI
SbSI
Sb(Se,S)I
(Sb,Bi)SeI
...

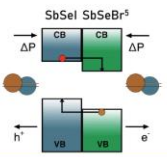

New synthesis routes

PVD: Co-evaporation

Solution-based:
- SbI_3 deposition on Sb_2Se_3 films
- Single-source precursors

[5] KT Butler, JM Frost, A Walsh, *Energy & Environmental Science*, 2015, 8, 838

ACKNOWLEDGEMENTS

Prof. Edgardo Saucedo

Prof. Marcel Placidi

UNIVERSITAT POLITÈCNICA DE CATALUNYA BARCELONATECH

UPC – PV group

This project has received funding from the European Research Council (ERC) under the European Union's Horizon 2020 research and innovation programme (grant agreement No 866018)

SENSATE

15

THANK YOU FOR YOUR ATTENTION

SENSATE

16

Appendix C:

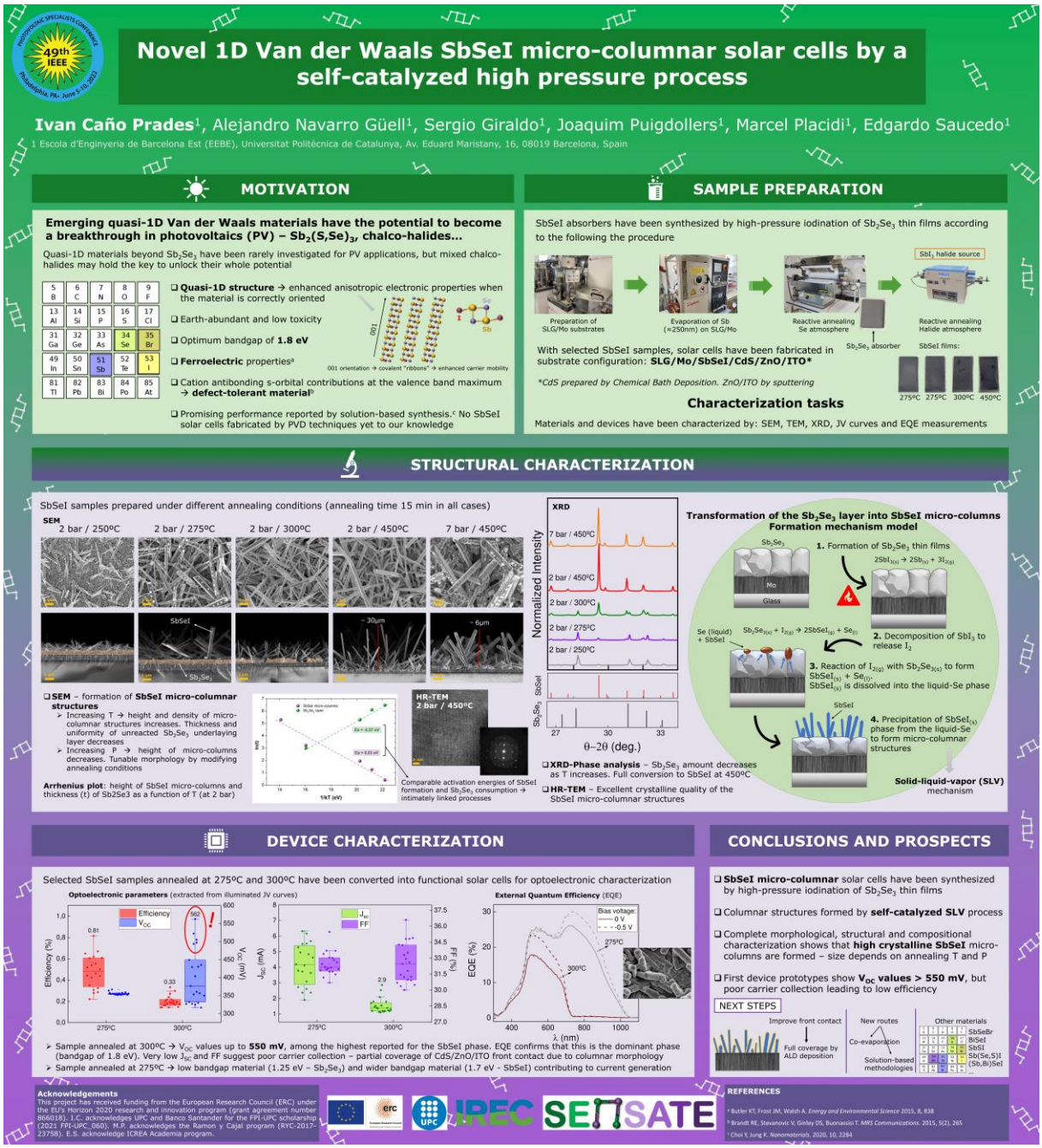
Novel 1D Van der Waals SbSeI micro-columnar solar cells by a self-catalyzed high pressure process
Ivan Caño Prades[1], Alejandro Navarro Güell[1], Sergio Giraldo[1], Joaquim Puigdollers[1], Marcel Placidi[1], Edgardo Saucedo[1]
1 Escola d'Enginyeria de Barcelona Est (EEBE), Universitat Politècnica de Catalunya, Av. Eduard Maristany, 16, 08019 Barcelona, Spain
MOTIVATION
Emerging quasi-1D Van der Waals materials have the potential to become a breakthrough in photovoltaics (PV) – Sb2(S,Se)3, chalco-halides...
Quasi-1D materials beyond Sb2Se3 have been rarely investigated for PV applications, but mixed chalco-halides may hold the key to unlock their whole potential
Quasi-1D structure → enhanced anisotropic electronic properties when the material is correctly oriented
Earth-abundant and low toxicity
Optimum bandgap of 1.8 eV
Ferroelectric properties[3]
Cation antibonding s-orbital contributions at the valence band maximum → defect-tolerant material[3]
Promising performance reported by solution-based synthesis.[c] No SbSeI solar cells fabricated by PVD techniques yet to our knowledge
001 orientation → covalent "ribbons" → enhanced carrier mobility
SAMPLE PREPARATION
SbSeI absorbers have been synthesized by high-pressure iodination of Sb2Se3 thin films according to the following procedure
Preparation of SLG/Mo substrates
Evaporation of Sb (≈250nm) on SLG/Mo
Reactive annealing Se atmosphere
Reactive annealing Halide atmosphere
SbI3 halide source
Sb2Se3 absorber
SbSeI films:
275ºC 275ºC 300ºC 450ºC
With selected SbSeI samples, solar cells have been fabricated in substrate configuration: SLG/Mo/SbSeI/CdS/ZnO/ITO*
*CdS prepared by Chemical Bath Deposition. ZnO/ITO by sputtering
Characterization tasks
Materials and devices have been characterized by: SEM, TEM, XRD, JV curves and EQE measurements
STRUCTURAL CHARACTERIZATION
SbSeI samples prepared under different annealing conditions (annealing time 15 min in all cases)
SEM
2 bar / 250ºC
2 bar / 275ºC
2 bar / 300ºC
2 bar / 450ºC
7 bar / 450ºC
SbSeI
Sb2Se3
~ 30µm
~ 6µm
SEM – formation of SbSeI micro-columnar structures
Increasing T → height and density of micro-columnar structures increases. Thickness and uniformity of unreacted Sb2Se3 underlaying layer decreases
Increasing P → height of micro-columns decreases. Tunable morphology by modifying annealing conditions
Arrhenius plot: height of SbSeI micro-columns and thickness (t) of Sb2Se3 as a function of T (at 2 bar)
Ea = 0.67 eV
Ea = 1.03 eV
1/kT (eV)
HR-TEM
2 bar / 450ºC
Comparable activation energies of SbSeI formation and Sb2Se3 consumption → intimately linked processes
XRD
7 bar / 450ºC
2 bar / 450ºC
2 bar / 300ºC
2 bar / 275ºC
2 bar / 250ºC
Normalized Intensity
SbSeI
Sb2Se3
θ–2θ (deg.)
XRD-Phase analysis – Sb2Se3 amount decreases as T increases. Full conversion to SbSeI at 450ºC
HR-TEM – Excellent crystalline quality of the SbSeI micro-columnar structures
Transformation of the Sb2Se3 layer into SbSeI micro-columns Formation mechanism model
Sb2Se3
Mo
Glass
1. Formation of Sb2Se3 thin films
2SbI3(s) → 2Sb(s) + 3I2(g)
2. Decomposition of SbI3 to release I2
Se (liquid) + SbSeI
Sb2Se3(s) + I2(g) → 2SbSeI(s) + Se(l)
3. Reaction of I2(g) with Sb2Se3(s) to form SbSeI(s) + Se(l). SbSeI(s) is dissolved into the liquid-Se phase
SbSeI
4. Precipitation of SbSeI(s) phase from the liquid-Se to form micro-columnar structures
Solid-liquid-vapor (SLV) mechanism
DEVICE CHARACTERIZATION
Selected SbSeI samples annealed at 275ºC and 300ºC have been converted into functional solar cells for optoelectronic characterization
Optoelectronic parameters (extracted from illuminated JV curves)
Efficiency
Voc
Jsc
FF
External Quantum Efficiency (EQE)
Bias voltage:
0 V
-0.5 V
275ºC
300ºC
λ (nm)
Sample annealed at 300ºC → Voc values up to 550 mV, among the highest reported for the SbSeI phase. EQE confirms that this is the dominant phase (bandgap of 1.8 eV). Very low Jsc and FF suggest poor carrier collection – partial coverage of CdS/ZnO/ITO front contact due to columnar morphology
Sample annealed at 275ºC → low bandgap material (1.25 eV – Sb2Se3) and wider bandgap material (1.7 eV - SbSeI) contributing to current generation
CONCLUSIONS AND PROSPECTS
SbSeI micro-columnar solar cells have been synthesized by high-pressure iodination of Sb2Se3 thin films
Columnar structures formed by self-catalyzed SLV process
Complete morphological, structural and compositional characterization shows that high crystalline SbSeI micro-columns are formed – size depends on annealing T and P
First device prototypes show Voc values > 550 mV, but poor carrier collection leading to low efficiency
NEXT STEPS
Improve front contact
Full coverage by ALD deposition
New routes
Co-evaporation
Solution-based methodologies
Other materials
SbSeBr
BiSeI
SbSI
Sb(Se,S)I
(Sb,Bi)SeI
Acknowledgements
This project has received funding from the European Research Council (ERC) under the EU's Horizon 2020 research and innovation program (grant agreement number 866018). I.C. acknowledges UPC and Banco Santander for the FPI-UPC scholarship (2021 FPI-UPC_060). M.P. acknowledges the Ramon y Cajal program (RYC-2017-23758). E.S. acknowledge ICREA Academia program.
REFERENCES
[1] Butler KT, Frost JM, Walsh A. Energy and Environmental Science 2015, 8, 838
[2] Brandt RE, Stevanovic V, Ginley DS, Buonassisi T. MRS Communications. 2015, 5(2), 265
[3] Choi Y, Jung K. Nanomaterials. 2020, 10, 2284